

Asteroseismology of the dip structure in period-spacings of rapidly rotating γ Doradus stars caused by the coupling between core and envelope oscillations

Takato Tokuno,^{1 2*} Masao Takata¹

¹ Department of Astronomy, School of Science, The University of Tokyo, 7-3-1 Hongo, Bunkyo-ku, Tokyo 113-0033, Japan

² Graduate School of Arts & Sciences, The University of Tokyo, 3-8-1 Komaba, Meguro, Tokyo 153-8902, Japan

Accepted XXX. Received YYY; in original form ZZZ

ABSTRACT

Recent asteroseismic observations by the *Kepler* space mission have revealed the dip fine structure in the period-spacing versus period diagram of rapidly rotating γ Doradus stars. Following the successful reproduction of the dip structure by numerical calculations in previous studies, we present in this paper the physical mechanism of how the dip is formed as a result of the interaction between the gravito-inertial waves in the radiative envelope and the pure inertial waves in the convective core. We analytically describe the wave solutions in both of the radiative envelope and the convective core, and match them at the interface to construct an eigenmode. We have found from the analysis the following points: the dip structure is mainly controlled by a parameter that has an inverse correlation with Brunt–Väisälä frequency at the interface; the depth and the width of the dip is shallower and larger, respectively, as the parameter gets large; the shape of the dip can be approximated by the Lorentzian function; the period at the central position of the dip is equal to or slightly smaller than that of the involved pure inertial mode in the convective core. We have also understood based on the evolutionary models of main-sequence stars that the parameter is inversely correlated with the chemical composition gradient at the convective-core boundary. The dip structure thus would provide information about the poorly-understood physical processes, such as diffusion, convective overshooting and rotational mixing, around the boundary between the convective core and the radiative envelope.

Key words: Asteroseismology – stars: interiors — stars: oscillations — stars: rotation — stars: variables:general .

1 INTRODUCTION

Theory of stellar structure and evolution is one of the cornerstones in our understanding of the universe. It is involved in a lot of key problems in astrophysics, including nucleosynthesis (and hence chemical evolution), galactic archaeology, and the dynamo mechanism to generate and maintain the magnetic field. The conventional approach to study stellar physics is to compare the observed surface properties of stars, such as effective temperature, gravity and chemical compositions, with the theoretical models that are constructed based on fundamental physical laws. While this method has been fairly successful in describing the global picture of stellar evolution, there still remain some important questions. Particularly, we have poorly understood the details of the physical processes that are related to convection, rotation and the magnetic field in the stellar interior (e.g. [Kippenhahn et al. 2012](#); [Maeder 2009](#)).

Asteroseismology is a relatively new and rapidly growing field in stellar physics. It aims to probe the internal structure of stars with the oscillations detected at the surface. Thanks to recent space missions such as CoRoT ([Baglin et al. 2006](#)), *Kepler* ([Borucki et al. 2010](#)) and TESS ([Ricker et al. 2014](#)), we have obtained massive and high-quality seismic data of a variety of pulsating variable stars. These data make

it possible to study the unresolved problems in stellar physics from a different angle.

One of the long-standing problems in the theory of stellar structure and evolution is that of rotation. It is coupled with various types of hydrodynamical and magnetohydrodynamical instabilities, and accordingly induces the transport and mixing of materials. The redistribution of chemical elements that are involved in nuclear reactions directly affects nucleosynthesis, the evolutionary track on the HR diagram, and the lifetime of the stars. It is also considered to play an essential role in generating and maintaining the magnetic field in the stars.

We confine ourselves in this paper to the γ Doradus (γ Dor) stars ([Cousins 1992](#); [Balona et al. 1994](#); [Krisciunas 1994](#)). They are main-sequence stars with the mass of 1.4–2.0 M_{\odot} and the typical rotation period of about 1 day. They exhibit oscillations with multiple periods of about 1 day (e.g. [Li et al. 2020](#)), which is comparable to their typical rotation period. Since the dynamical time-scale of these stars is about a few hours, we understand that the oscillations are non-radial high-order gravity modes, but with the considerable impact of rotation. In fact, recent studies have demonstrated that the main contribution to their oscillation spectrum comes from the gravito-inertial modes, which are composed of gravity waves strongly affected by the Coriolis force ([Van Reeth et al. 2015](#); [Saio et al. 2018a,b](#)). More specifically, [Li et al. \(2020\)](#) have shown that the most commonly observed modes in γ Dor stars are Kelvin g modes (or prograde sectoral

* E-mail: tokuno-takato@g.ecc.u-tokyo.ac.jp (TT)

g modes), and that Rossby modes (or r modes; Papaloizou & Pringle 1978) are also detected in about 20 per cent of the stars in their sample. Once we identify the observed eigenmodes and understand their physical properties, we may interpret the observed oscillation spectrum in terms of a few structural parameters, including the average rotation period heavily weighted in the deep radiative region and the characteristic period of the oscillations (Van Reeth et al. 2016; Christophe et al. 2018; Li et al. 2020; Takata et al. 2020a,b).

High-precision data from the *Kepler* mission further allow us to examine the fine structure in the frequency spectrum of γ Dor stars. Saio et al. (2018b) have noticed in the analysis of KIC 5608334 that the distribution of period-spacings deviates in a small period range from the one expected by Kelvin g modes trapped in the radiative envelope, though they misinterpret that the structure is caused by the interaction with other types of gravito-inertial modes, which are also confined in the radiative envelope. Ouazzani et al. (2020) have then shown based on numerical calculations that the eigenmodes in the relevant period range have finite amplitude not only in the radiative envelope, but also in the convective core, where the buoyancy force does not exist. They have interpreted these modes to consist of the pure inertial waves in the convective core, which are restored by only the Coriolis force, and the gravito-inertial waves in the radiative envelope. The numerical calculations by Saio et al. (2018b) and those by Ouazzani et al. (2020) agree that the period-spacings are smaller in the relevant period range so that their distribution follows a characteristic dip structure. In fact, Saio et al. (2021) have identified such dips in a sample of γ Dor stars observed by the *Kepler* mission, and succeeded in constraining the rotation period of the convective core by constructing the evolutionary model of each star that has consistent dip structure with the observations.

While Saio et al. (2021) have clearly demonstrated the potential of asteroseismology based on the dip structure in the period-spacing distribution to diagnose the properties of the convective core of γ Dor stars, it is fair to say that the physical mechanism to form the dip structure is yet to be made clear in detail. The main purpose of this paper is to treat this problem based on the analytical approach rather than the numerical one adopted by Ouazzani et al. (2020) and Saio et al. (2021). By this approach, we can elucidate which physical parameters are most important for the dip formation, and discuss how these parameters depend on the mass and the evolutionary stage.

The outline of this paper follows. In Section 2, we first propose the general picture of the dip formation without any detailed analysis. In Section 3, we analytically formulate the problem of eigenoscillation by matching the pure inertial waves in the convective core with the gravito-inertial waves in the radiative envelope. Solving the problem approximately, we make clear the properties of the dip structure in the period-spacing versus period diagram. In Section 4, we compare the derived expressions with the results of numerical calculations to investigate the evolutionary change of the dip structure during the main-sequence stage and to confirm the validity of the approximated expressions. Discussions and conclusions are presented in Sections 5 and 6, respectively.

2 PICTURE OF THE DIP FORMATION

In this section, we propose a physical picture to explain how the dip structure in a period-spacing (ΔP) versus period (P) diagram is formed as a result of the interaction between the pure-inertial waves in the convective core and the gravito-inertial waves in the radiative envelope. Our argument consists of three steps.

In the first step, we consider the case where the oscillations are

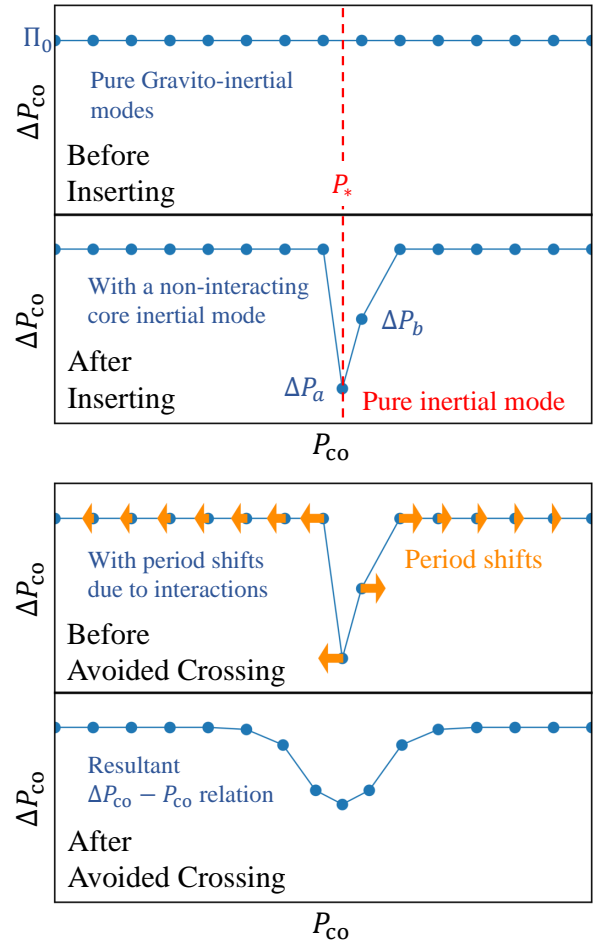


Figure 1. Schematic pictures of dip formation in the P - ΔP diagram, where the period P and the period spacing ΔP are both measured in the co-rotating frame. Upper panel (step 1 and 2): a pure-inertial mode is inserted in the spectrum of the constant period-spacing of the gravito-inertial modes. Lower panel (step 3): the dip is formed as a result of the avoided crossing.

completely evanescent in the convective core irrespective of the frequency, so that there exist only gravito-inertial modes trapped in the radiative envelope. Among those modes, we concentrate on Kelvin g modes (or prograde sectoral g modes) because they have the highest visibility in a rapidly rotating star. The oscillation periods of these modes are (almost) equally spaced in the co-rotating frame. Therefore, the corresponding period-spacing ΔP is constant (with a constant period-spacing of Π_0), as shown in the top panel of Figure 1. This property of the Kelvin modes is totally analogous to that of the high-order g modes in the absence of rotation.

We next take account of the pure inertial modes that are confined in the convective core, but have no interaction with the envelope oscillations. Because the frequency spectrum of those modes are much more sparse than the Kelvin g modes, we may pay attention to only one pure-inertial mode. If the period of the pure-inertial mode P_* lies between the two consecutive periods P_a and P_b of the gravito-inertial modes, the two period-spacings $\Delta P_a = P_* - P_a$ and $\Delta P_b = P_b - P_*$ are smaller than Π_0 , whereas the other period-spacings remain to be Π_0 . This is shown in the second panel of Figure 1.

In the final step, we consider the interaction between two consecutive modes. We may regard that the interaction causes the mode periods to repulse each other (cf. the second last panel of Figure 1). This phenomenon is essentially the same as the avoided crossing (cf. Osaki 1975; Aizenman et al. 1977). Since the repulsing force should be stronger if the two periods are closer to each other, the period-spacings near P_* get larger because of interaction, whereas those far from P_* are hardly changed. The P - ΔP diagram is accordingly modified so that the two small values ΔP_a and ΔP_b get slightly larger, and other values close to them become smaller than Π_0 . We thus observe the formation of a dip as in the bottom panel of Figure 1.

Based on the presented picture, we may derive a simple relation of the period-spacings. For this purpose, let us evaluate the sum of the period-spacings in a wide range of the period that includes the dip. If the mode periods including P_* in the range are expressed by P_n with the integral indices n in the range of $n_{\min} \leq n \leq n_{\max}$, where the smaller values of n correspond to the shorter periods, the period-spacing is defined as

$$\Delta_n P = P_{n+1} - P_n, \quad (1)$$

so that its sum is given by

$$\sum_{n=n_{\min}}^{n_{\max}-1} \Delta_n P = P_{n_{\max}} - P_{n_{\min}}. \quad (2)$$

Since the mode periods are scarcely changed by the interaction if they are far from P_* , the difference on the right-hand side of equation (2) can be calculated based on the period spectrum of the gravito-inertial modes, which essentially has the constant spacing of Π_0 . Because there are in total $n_{\text{tot}} = n_{\max} - n_{\min} + 1$ modes in the range, the numbers of the gravito-inertial modes and their period-spacings are $n_{\text{tot}} - 1$ and $n_{\text{tot}} - 2$, respectively. We therefore obtain $\sum_n \Delta_n P \approx (n_{\text{tot}} - 2)\Pi_0$, which is equivalent to

$$\sum_{n=n_{\min}}^{n_{\max}-1} \left(1 - \frac{\Delta_n P}{\Pi_0}\right) \approx 1. \quad (3)$$

3 FORMULATION AND ANALYSIS

This section shows our analysis about the resonance of the waves between the convective core and radiative envelope. We first formulate the expressions of oscillations in the envelope (Section 3.1.1) and the (uniform density) core (Section 3.1.2) separately. We consider the uniform density core because the analytical solutions are exceptionally known for this case.

Then, we match the oscillations in the two regions by requiring the continuity of the radial displacement ξ_r and the Lagrangian pressure perturbation δp at the boundary (Section 3.2). Solving the matching conditions approximately, we obtain an approximate relation between the oscillation period P and the period-spacing ΔP including the effect of coupling (Section 3.3). We additionally show that the analysis can formally be justified even if the core density is not uniform (Section 3.4).

Before starting the analysis, we make a remark about the structure near the boundary between the convective core and the radiative envelope. While we assume up to Section 3.4 that the profiles of the hydrogen mass fraction X_H and hence the density ρ are continuous at the boundary, we then present an analysis for the case when these profiles are discontinuous in Section 3.5. Fig 2 shows the schematic

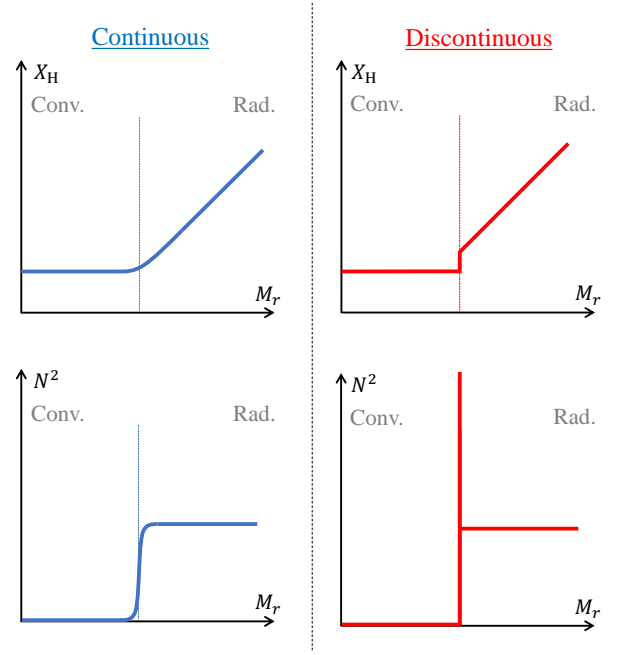


Figure 2. Schematic profiles of the hydrogen mass fraction X_H and (squared) Brunt-Väisälä frequency N^2 for the continuous (left panels) and discontinuous (right panels) cases. The abscissas mean the concentric mass, while the ordinates correspond to X_H in the upper panels and N^2 in the lower panels. The vertical dashed lines represent the boundary between the convective core and the radiative envelope.

profiles of X_H and (squared) Brunt-Väisälä frequency N^2 to indicate the difference between the continuous and discontinuous cases.

From a physical point of view, we should apply the continuous (discontinuous) case if the scale height of N^2 at the boundary is much larger (smaller) than the local wavelength of gravito-inertial waves around the peak of N^2 in the radiative envelope. The reason why we consider the both cases is that the structure near the boundary is not understood well. We should determine which case should be applied depending the evolutionary stage and the physical processes considered.

3.1 Equation of oscillations

The fundamental equations of the present analysis are those of linear adiabatic oscillations of rotating stars. We assume that the equilibrium structure is spherically symmetric, which is a good approximation for low-frequency oscillations trapped mainly in the deep interior of the stars. We also assume for simplicity uniform rotation.

3.1.1 Envelope oscillations

The oscillations in the envelope of γ Dor stars are composed of gravito-inertial waves, of which restoring force is the buoyancy combined with the Coriolis force. Those oscillations can be described accurately by the traditional approximation of rotation (TAR) (e.g. Eckart 1960; Aerts et al. 2010). In this framework, we neglect the horizontal component of the angular velocity of rotation and the perturbation to the gravitational potential (the Cowling approximation). The most important point is that the oscillation variables under TAR are separable in the spherical coordinates (r, θ, ϕ) in the co-rotating frame. The radial displacement ξ_r and the Eulerian pressure

perturbation p' can be written as

$$\xi_r = \xi_r(r) \Theta_k^m(\mu; s) e^{im\phi - i\omega t} \quad (4)$$

and

$$p' = p'(r) \Theta_k^m(\mu; s) e^{im\phi - i\omega t}, \quad (5)$$

respectively. Here, $\xi_r(r)$ and $p'(r)$ stand for the parts of radial dependence. The axial symmetry of the equilibrium structure leads to the azimuthal dependence of $e^{im\phi}$, where m is the azimuthal order. Since we choose the time (t) dependence of $e^{-i\omega t}$, positive (negative) values of m correspond to prograde (retrograde) modes. On the other hand, the θ dependence (through $\mu = \cos\theta$) is described by the Hough function, $\Theta_k^m(\mu; s)$, which is the eigenfunction of the Laplace tidal equation. The integral index k is introduced by Lee & Saio (1997) to distinguish the kind of modes, and the spin parameter s is defined by $s = 2\Omega/\omega$, in which Ω is the angular velocity of rotation.

The radial parts of the variables satisfy

$$\frac{d\xi_r(r)}{dr} = -\left(\frac{2}{r} - \frac{1}{\Gamma_1 H_p}\right) \xi_r(r) + \frac{1}{\rho c_s^2} \left(\frac{\lambda c_s^2}{r^2 \omega^2} - 1\right) p'(r), \quad (6)$$

and

$$\frac{dp'(r)}{dr} = \rho (\omega^2 - N^2) \xi_r(r) - \frac{p'(r)}{\Gamma_1 H_p}, \quad (7)$$

where H_p , N , Γ_1 , ρ and c_s mean the pressure scale height, the Brunt-Väisälä frequency, the first adiabatic index, the density and the sound speed, respectively. Equations (6) and (7) have the same form as the oscillation equations of non-rotating stars under the Cowling approximation. Only the difference is that, in the absence of rotation, the eigenvalue of the Laplace tidal equation, λ , is replaced with $\ell(\ell+1)$, where ℓ is the spherical degree. We can therefore analyse equations (6) and (7) in the same way as in the case without rotation.

Because the oscillation periods of γ Dor stars are much longer than the dynamical time-scale of the stars, the (radial) wavelengths of the constituent waves are short enough for the JWKB type asymptotic analysis to be applicable (cf. Unno et al. 1989, Section. 16). We first introduce new dependent variables v and w by

$$v \equiv \rho^{1/2} c_s r^2 \left| 1 - \frac{\lambda c_s^2}{r^2 \omega^2} \right|^{-1/2} \frac{\xi_r(r)}{r}. \quad (8)$$

and

$$w \equiv \rho^{1/2} c_s^2 r \left| N^2 - \omega^2 \right|^{-1/2} \frac{p'(r)}{\rho c_s^2}, \quad (9)$$

respectively. We can show from equations (6) and (7) that v and w satisfy

$$\frac{d^2 v}{dr^2} + k_r^2 v \simeq 0 \quad (10)$$

and

$$\frac{d^2 w}{dr^2} + k_r^2 w \simeq 0, \quad (11)$$

respectively, where k_r denotes the wave number defined as

$$k_r^2 \equiv \frac{\omega^2 - N^2}{c_s^2} \left(1 - \frac{\lambda c_s^2}{r^2 \omega^2} \right). \quad (12)$$

The solutions of equation (10) and (11) are propagative (evanescent) if k_r^2 is positive (negative). We mainly consider the case of $\lambda > 0$ in this paper, and assume that the radiative envelope consists of one big propagative region and surrounding small evanescent

regions. The inner and outer boundaries of the propagation region (turning points) are denoted by r_a and r_b , respectively. Practically, r_a is determined by the condition of $\omega = N$, and is almost equal to the radius of the convective core boundary (cf. Fig. A1 in Appendix A). On the other hand, r_b is fixed by $\omega = \min(N, L)$, where $L \equiv \sqrt{\lambda} c_s / r$ denotes the Lamb frequency, and is very close to the stellar surface.

The reason for introducing the two dependent variables rather than one is that neither of the solutions of equations (10) and (11) is valid in the entire range. This is because the neglected terms on the right-hand side of equations (10) and (11) diverge at $r = r_b$ and $r = r_a$, respectively. General solutions of the differential equations can be given as

$$v \simeq \frac{1}{\sqrt{|k_r|}} \left(\frac{3}{2} \left| \int_{r_a}^r |k_r| dr \right| \right)^{1/6} \times [a \text{Ai}(\zeta_1) + b \text{Bi}(\zeta_1)] \quad \text{for } r \ll r_b \quad (13)$$

and

$$w \simeq \frac{1}{\sqrt{|k_r|}} \left(\frac{3}{2} \left| \int_r^{r_b} |k_r| dr \right| \right)^{1/6} \times [c \text{Ai}(\zeta_2) + d \text{Bi}(\zeta_2)] \quad \text{for } r_a \ll r. \quad (14)$$

Here $\text{Ai}(x)$ and $\text{Bi}(x)$ are the Airy functions of the first and second kind, respectively, and ζ_1 and ζ_2 are defined as

$$\zeta_1 \equiv \text{sgn}(k_r^2) \left(\frac{3}{2} \left| \int_{r_a}^r |k_r| dr \right| \right)^{2/3} \quad (15)$$

and

$$\zeta_2 \equiv \text{sgn}(k_r^2) \left(\frac{3}{2} \left| \int_r^{r_b} |k_r| dr \right| \right)^{2/3}, \quad (16)$$

respectively. Arbitrary constants a , b , c and d (in equations 13 and 14) should be constrained by the boundary conditions. Following Unno et al. (1989), we adopt the convention that $\text{Ai}(\zeta)$ and $\text{Bi}(\zeta)$ are the solutions of

$$\frac{d^2 y}{d\zeta^2} + \zeta y = 0. \quad (17)$$

From the condition that w should decay exponentially for $r \gg r_b$, we first obtain $d = 0$. Then, matching the asymptotic form of w with that of v for $r_a \ll r \ll r_b$ based on $|k_r w| \simeq |dv/dr|$, we find

$$a = -c \sin B \quad (18)$$

and

$$b = -c \cos B, \quad (19)$$

where

$$B \equiv \int_{r_a}^{r_b} k_r dr - \frac{\pi}{2} \simeq \frac{\pi^2 s}{\Omega \Pi_0} - \frac{\pi}{2}. \quad (20)$$

Here Π_0 denotes the asymptotic period-spacing of the gravito-inertial modes, which is defined as

$$\Pi_0 \simeq \frac{2\pi^2}{\sqrt{\lambda}} \left(\int_{r_a}^{r_b} N \frac{dr}{r} \right)^{-1}, \quad (21)$$

and the most right-hand side of equation (20) is derived from equation (12) under the approximations of $\omega \ll \sqrt{\lambda} c_s / r$ and $\omega \ll N$ for $r_a \ll r \ll r_b$. Now, we regard Π_0 as the constant for $s \gg 1$ because (1) integration over $r_a \leq r \leq r_b$ can essentially be interpreted as that over the whole radiative zone, and (2) the variation of λ is small (for Kelvin g modes). This assumption will be discussed in Section 5.4 and Appendix A.

The final step of the analysis in this section is to derive the expression of ξ_r and p' at the inner boundary of the radiative envelope, which we denote by R_{core} . Because r_a is very close to R_{core} , we may alternatively evaluate those variables at $r = r_a$ (This approximation will be justified in more detail at the end of this section). For this purpose, we use equation (12) to expand k_r^2 near $r = r_a$ as

$$k_r^2 \simeq \left[\frac{\lambda}{r^2 \omega^2} \frac{dN^2}{dr} \right]_{r=r_a} (r - r_a) = \frac{\lambda s^2}{\epsilon^3 r_a^3} (r - r_a), \quad (22)$$

in which we have utilised $N \simeq \omega$ and $\omega \ll \sqrt{\lambda} c_s / r$. We have also introduced the parameter ϵ by

$$\epsilon \equiv \left(\frac{r_a}{4\Omega^2} \frac{dN^2}{dr} \Big|_{r=r_a} \right)^{-1/3}, \quad (23)$$

and assume $\epsilon \ll 1$ because N steeply increases just outside the convective core (cf. Section 4).

We can then derive from equation (22) the following relations:

$$\lim_{r \rightarrow r_a} \frac{1}{\sqrt{|k_r|}} \left(\frac{3}{2} \int_{r_a}^r |k_r| dr \right)^{1/6} = \frac{\epsilon^{1/2} r_a^{1/2}}{s^{1/3} \lambda^{1/6}}, \quad (24)$$

$$\lim_{r \rightarrow r_a} \frac{d}{dr} \left[\frac{1}{\sqrt{|k_r|}} \left(\frac{3}{2} \int_{r_a}^r |k_r| dr \right)^{1/6} \right] = 0 \quad (25)$$

and

$$\lim_{r \rightarrow r_a} \frac{d\xi_1}{dr} = \frac{s^{2/3} \lambda^{1/3}}{\epsilon r_a}. \quad (26)$$

In addition, we rewrite equation (6) using equation (8) as

$$\frac{p'(r)}{p\Gamma_1} = \frac{\omega}{c_s^2 \lambda^{1/2} \rho^{1/2}} \left[\frac{dv}{dr} - \left(\frac{1}{2} \frac{d \ln \rho}{dr} - \frac{1}{\Gamma_1} \frac{d \ln p}{dr} \right) v \right]. \quad (27)$$

From equations (8), (13), (24)–(26) and (27), we finally obtain the expressions of ξ_r and p' at $r = r_a$ in the leading order of ϵ as

$$\frac{\xi_r(r)}{r} \Big|_{r=r_a} \simeq Q \epsilon X(s), \quad (28)$$

$$\frac{p'(r)}{p\Gamma_1} \Big|_{r=r_a} \simeq Q \frac{r_a^2 \omega^2}{c_s^2} Y(s), \quad (29)$$

respectively, where we have introduced

$$X(s) \equiv \lambda^{1/6} s^{2/3} \sin \left(\frac{\pi^2 s}{\Omega \Pi_0} - \frac{\pi}{6} \right) \quad (30)$$

and

$$Y(s) \equiv \alpha \lambda^{-1/2} s^{4/3} \sin \left(\frac{\pi^2 s}{\Omega \Pi_0} - \frac{5\pi}{6} \right). \quad (31)$$

The dimensionless parameters α and Q are defined as

$$\alpha \equiv \frac{3^{1/3} \Gamma(2/3)}{\Gamma(1/3)} \approx 0.73, \quad (32)$$

$$Q \equiv - \frac{c}{3^{2/3} \Gamma(2/3)} \frac{\lambda^{1/6}}{\epsilon^{1/2} \Omega r_a^{5/2}} \frac{1}{\rho^{1/2}} \Big|_{r=r_a}, \quad (33)$$

respectively. Since c in equations (13) and (14) is an arbitrary constant, Q in equations (28) and (29) can be regarded as the normalisation constant.

Now we should confirm that the values of ξ_r and p' at $r = r_a$ are sufficiently close to those at $r = R_{\text{core}}$, where they are fitted with an inertial oscillation in the core. Using $N^2|_{r=R_{\text{core}}} = 0$, $N^2|_{r=r_a} = \omega^2$ and equation (23), we can show

$$\frac{R_{\text{core}}}{r_a} \sim 1 - \frac{\epsilon^3}{s^2}, \quad (34)$$

and then, from the Taylor expansion, we can derive

$$\frac{v|_{r=R_{\text{core}}}}{v|_{r=r_a}} \sim 1 + \mathcal{O}(\epsilon^2/s^{4/3}). \quad (35)$$

Considering $s \sim 10$, we conclude that v at $r = r_a$ is different from that at $r = R_{\text{core}}$ only in the second order of ϵ .

Equations (28) and (29) are for $\Theta_k^m(\mu; s)$ with a given k (λ at a given s depends on k). In order to fit them with a core oscillation having a different θ dependence (but the common $e^{im\phi - i\omega t}$ dependence), we construct general solutions by linear combinations as

$$\frac{\xi_r}{r} \Big|_{r=R_{\text{core}}} = \sum_k a_k \epsilon X_k(s) \Theta_k^m(\mu; s) \quad (36)$$

and

$$\frac{p'}{p\Gamma_1} \Big|_{r=R_{\text{core}}} = \frac{\omega^2 R_{\text{core}}^2}{c_s^2} \sum_k a_k Y_k(s) \Theta_k^m(\mu; s), \quad (37)$$

in which the normalisation constant Q has been absorbed by the coefficient a_k .

3.1.2 Core oscillations (in the case of uniform density)

The oscillations trapped in the convective core of γ Dor stars are composed of inertial waves, for which the Coriolis force is the restoring force. We formulate pure inertial modes in this section based on Wu (2005).

The equations of linear adiabatic oscillations of the convective core (with $N = 0$) in the co-rotating frame can be recast under the Cowling approximation into a single equation of the scalar variable ψ , which is defined as

$$\psi \equiv \frac{1}{\omega^2} \frac{p'}{\rho}. \quad (38)$$

If the density is uniform, the governing equation is reduced to

$$\nabla^2 \psi - s^2 \frac{\partial^2 \psi}{\partial z^2} = 0. \quad (39)$$

This equation is separable in the ellipsoidal coordinates, and the solutions are given by the products of two associated Legendre functions with the same indices (Bryan 1889). Assuming that ξ_r and p' depend on t and ϕ through $e^{im\phi - i\omega t}$, we can show that they are related to ψ by

$$\xi_r = \frac{1}{1 - s^2} \left(\frac{\partial}{\partial r} - \frac{ms}{r} - \mu s^2 \frac{\partial}{\partial z} \right) \psi \quad (40)$$

and

$$p' = p\Gamma_1 \frac{\omega^2}{c_s^2} \psi. \quad (41)$$

From these relations, we obtain the corresponding expressions at the outer boundary of the core as¹

¹ When we rewrite equation (40) in the ellipsoidal coordinate system, we have corrected equation (28) of Wu (2005) as

$$\xi_r = \frac{(1 - x_1^2)(1 - x_2^2)}{(1 - s^2)(x_1^2 - x_2^2)r} \left[x_1 \frac{\partial \psi}{\partial x_1} \frac{s^{-2} - x_2^2}{1 - x_2^2} - x_2 \frac{\partial \psi}{\partial x_2} \frac{s^{-2} - x_1^2}{1 - x_1^2} + \frac{m}{s} \frac{x_1^2 - x_2^2}{(1 - x_1^2)(1 - x_2^2)} \psi \right].$$

$$\left. \frac{\xi_r(r)}{r} \right|_{r=R_{\text{core}}} \propto C_\ell^m(1/s) P_\ell^m(\mu) \quad (42)$$

and

$$\left. \frac{p'(r)}{p\Gamma_1} \right|_{r=R_{\text{core}}} \propto \frac{R_{\text{core}}^2 \omega^2}{c_s^2} P_\ell^m(1/s) P_\ell^m(\mu), \quad (43)$$

where P_ℓ^m indicates the associated Legendre function, and C_ℓ^m is defined as

$$C_\ell^m(x) \equiv x \left(\frac{dP_\ell^m(x)}{dx} + \frac{m}{1-x^2} P_\ell^m(x) \right). \quad (44)$$

Here we require for pure inertial modes $\xi_r = 0$ at the outer boundary of the convective core. Then, the eigenmode condition can be expressed as $C_\ell^m(1/s) = 0$. Table 1 of [Ouazzani et al. \(2020\)](#) gives the eigenvalues $s = s_*$ for some values of m and ℓ .

By making linear combinations of equations (42) and (43) for different values of ℓ , we may obtain the general solutions as

$$\left. \frac{\xi_r}{r} \right|_{r=R_{\text{core}}} = \sum_\ell b_\ell C_\ell^m(1/s) \tilde{P}_\ell^m(\mu) \quad (45)$$

and

$$\left. \frac{p'}{p\Gamma_1} \right|_{r=R_{\text{core}}} = \frac{\omega^2 R_{\text{core}}^2}{c_s^2} \sum_\ell b_\ell P_\ell^m(1/s) \tilde{P}_\ell^m(\mu), \quad (46)$$

where b_ℓ are constant coefficients. Note that we have defined the normalised associated Legendre function by

$$\tilde{P}_\ell^m(x) \equiv \sqrt{\frac{(2\ell+1)! (\ell-m)!}{2(\ell+m)!}} P_\ell^m(x). \quad (47)$$

3.2 Matching the core and envelope solutions

We match the solutions in the radiative envelope with those in the convective core in this section. Hereafter, suffixes “rad” and “con” denote variables in the radiative zone and the convective zone.

We require that the radial displacement ξ_r and the Lagrangian pressure perturbation δp are continuous at the boundary between the two zones. Since we assume that the density ρ and its derivative $d\rho/dr$ of the equilibrium structure are continuous at the boundary, the continuity of δp can be replaced with that of the Eulerian pressure perturbation p' .

From equations (36), (37), (45) and (46), we can formulate the continuity conditions of $\xi_{r,\text{con}} = \xi_{r,\text{rad}}$ and $p'_{\text{rad}} = p'_{\text{con}}$ at $r = R_{\text{core}}$ as

$$\sum_k a_k \epsilon X_k(s) \Theta_k^m(\mu; s) = \sum_\ell b_\ell C_\ell^m(1/s) \tilde{P}_\ell^m(\mu) \quad (48)$$

and

$$\sum_k a_k Y_k(s) \Theta_k^m(\mu; s) = \sum_\ell b_\ell P_\ell^m(1/s) \tilde{P}_\ell^m(\mu), \quad (49)$$

respectively. If we multiply the both sides of equation (48) by $\Theta_{k'}^m(\mu; s)$, where k' is an integer, and integrate over $-1 \leq \mu \leq 1$, we obtain from the orthonormality of $\Theta_k^m(\mu; s)$ the expression of each $a_{k'}$, which can then be substituted into equation (49) to yield

$$[\mathcal{M}(s) - \epsilon \mathcal{N}(s)] \vec{b} = \vec{0}, \quad (50)$$

where \vec{b} is the vector whose ℓ -th element is equal to b_ℓ , and matrices \mathcal{M} and \mathcal{N} are defined as

$$[\mathcal{M}]_{k,\ell} = c_{k,\ell} Y_k(s) C_\ell^m(1/s) \quad (51)$$

and

$$[\mathcal{N}]_{k,\ell} = c_{k,\ell} X_k(s) P_\ell^m(1/s), \quad (52)$$

respectively. Here, we have introduced $c_{k,\ell}$ by

$$c_{k,\ell} \equiv \int_{-1}^1 \Theta_k^m(\mu; s) \tilde{P}_\ell^m(\mu) d\mu. \quad (53)$$

For \vec{b} to be non-trivial ($\vec{b} \neq \vec{0}$) in equation (50), we need to have

$$\det[\mathcal{M}(s) - \epsilon \mathcal{N}(s)] = 0, \quad (54)$$

which is the condition to determine s (and hence ω). Equation (50) can thus be regarded as the eigenvalue problem about s .

It is generally not easy to solve equation (50), which is a matrix equation of infinite dimension. We consider first the case of $\epsilon = 0$ separately, which corresponds to $dN^2/dr = \infty$ at R_{core} . Equation (54) is reduced in this case to (1) $Y_{k_0}(s) = 0$ for a certain value k_0 or (2) $C_{\ell_0}^m(1/s) = 0$ for a certain value of ℓ_0 . Case (1) corresponds to the eigenvector \vec{a} whose elements are equal to zero except for a_{k_0} . Then, we find from equations (48) and (49) $b_\ell = 0$ for all ℓ . The oscillation is a Kelvin g mode confined to the radiative envelope without being influenced from other modes. On the other hand, we may set in case (2) $b_{\ell_0} = 1$ and $b_\ell = 0$ for $\ell \neq \ell_0$. Then, equation (49) can be used to derive

$$a_k = \frac{c_{\ell_0,k} P_{\ell_0}^m(1/s)}{Y_k(s)}. \quad (55)$$

Although the solution corresponds to a pure-inertial mode in the convective core, it also has finite amplitude in the radiative envelope (and hence at the surface of the star) because $p' \neq 0$ at $r = R_{\text{core}}$. We note that the solutions for $\epsilon = 0$ (cases 1 and 2) correspond to independent oscillations with no avoided crossing as discussed in Section 2.

We thus understand that ϵ is the parameter to measure the strength of the interaction between the pure inertial modes in the convective core and the gravito-inertial modes in the radiative envelope. In order to solve equation (50) for $\epsilon \neq 0$, we make some simplifying assumptions. Firstly, the interaction between the oscillation in the core and that in the envelope is weak, so that $(0 <) \epsilon \ll 1$. Secondly, we consider in the interaction only one core mode and multiple envelope modes (with a single value of k) whose frequencies are close to that of the core mode. This is because the frequency spectrum of the pure inertial modes is much more sparse than that of the gravito-inertial modes, and the interaction is significant only between the core mode and the envelope modes with close frequencies.

Under these assumptions, we analyse equation (54) in the frequency range where the interaction is significant. If the core mode and the envelope modes, which are involved in the interaction, are specified by indices ℓ and k , respectively, we may assume that C_ℓ^m and Y_k are both of the order of ϵ , so that all the components in the ℓ -th column and the k -th row of matrix $\mathcal{M} - \epsilon \mathcal{N}$ are of the order of ϵ . Since the other components are of the order of unity, we can show from the cofactor expansion that equation (54) is satisfied in the leading order of ϵ if the (k, ℓ) component is equal to zero, which means

$$\frac{C_\ell^m(1/s) Y_k(s)}{P_\ell^m(1/s) X_k(s)} \simeq \epsilon. \quad (56)$$

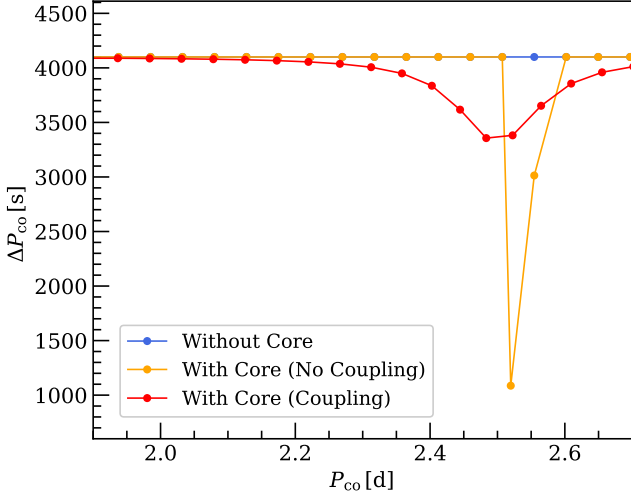


Figure 3. P - ΔP diagram (in the co-rotating frame) based on the solutions of equation (57). Blue, orange and red points represent those without the convective core, those with the core but no avoided crossing ($\epsilon = 0$), and those with both the core and avoided crossing ($\epsilon = 1/100$), respectively. Note that we set the rotation period $2\pi/\Omega = 0.455$ d and the period-spacing $\Pi_0 = 4100$ s.

Substitution of equations (30) and (31) into equation (56) leads to

$$F(s) \frac{\sqrt{3}}{2} \frac{\alpha}{\lambda^{2/3}} s^{2/3} \left[\cot\left(\frac{\pi^2 s}{\Omega \Pi_0} - \frac{\pi}{6}\right) + \frac{1}{\sqrt{3}} \right] \simeq \epsilon, \quad (57)$$

where $F(s)$ is defined as

$$F(s) \equiv -\frac{C_\ell^m(1/s)}{P_\ell^m(1/s)}. \quad (58)$$

In Fig. 3, we plot the relation between the oscillation period P and the period-spacing ΔP , which are computed numerically for $\ell = 3$ ² and $k = 0$ (Kelvin g modes) based on equation (57). We note that $F(s)$ is given by

$$F(s) = -\frac{s^2 - 10s - 15}{(s+1)(s^2-5)} \quad \text{for } \ell = 3 \text{ and } k = 0. \quad (59)$$

3.3 Approximated solutions

In order to derive an approximate analytic expression of the period-spacing ΔP in the co-rotating frame, we may further rewrite equation (57) by expanding $F(s)$ near its zero point $s = s_*$, which corresponds to the spin parameter of a pure inertial mode in the core, up to the linear term in s . We thus obtain

$$-V(s - s_*) \left[\cot\left(\frac{\pi^2 s}{\Omega \Pi_0} - \frac{\pi}{6}\right) + \frac{1}{\sqrt{3}} \right] \simeq \epsilon, \quad (60)$$

where

$$V \equiv \left[-\frac{dF(s)}{ds} \frac{\sqrt{3}}{2} \frac{\alpha s^{2/3}}{\lambda^{2/3}} \right]_{s=s_*}. \quad (61)$$

² In the case of uniform density core, the pure inertial mode with $\ell = 1$ is not considered because it corresponds to the displacement of the whole star with $\omega = 0$.

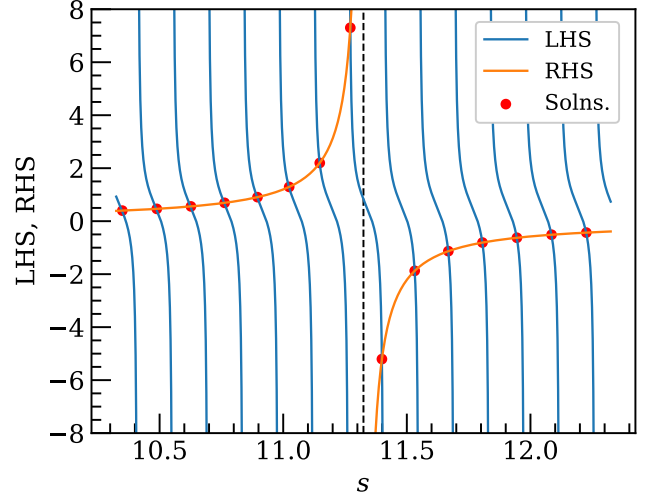


Figure 4. Solutions of equations (62). The horizontal axis represents spin parameter s . Blue and orange lines denote the left-hand side and the right-hand side of the equation, respectively. Red points represent the points of intersection between them. Black vertical dashed line indicates $s = s_*$.

Considering s_1 and s_2 as two neighbouring solutions of equation (60) with $s_1 > s_2$, we obtain

$$\cot\left(\frac{\pi^2 s_i}{\Omega \Pi_0} - \frac{\pi}{6}\right) + \frac{1}{\sqrt{3}} \simeq -\frac{\epsilon/V}{s_i - s_*} \quad (i = 1, 2), \quad (62)$$

Because the intersections between the left-hand side and the right-hand side with $s = s_1$ and s_2 are located on two adjacent branches of the cotangent function³ (see Fig. 4), we premise $\pi^2(s_1 - s_2)/\Omega \Pi_0 - \pi \ll 1$, which physically means that the frequency spectrum of the envelope modes is very dense. Then, by Taylor expansion, we acquire

$$\left[1 + \left(\frac{\epsilon/V}{\bar{s} - s_*} + \frac{1}{\sqrt{3}} \right)^2 \right] \left[\frac{\pi^2(s_1 - s_2)}{\Omega \Pi_0} - \pi \right] \simeq -\frac{\epsilon}{V} \frac{s_1 - s_2}{(\bar{s} - s_*)^2}, \quad (63)$$

in which $\bar{s} = (s_1 + s_2)/2$. Rewriting equation (63) with $P = \pi \bar{s}/\Omega$, $\Delta P = \pi(s_1 - s_2)/\Omega$, $P_* = \pi s_*/\Omega$ and a new parameter

$$\sigma \equiv \frac{3\pi\epsilon}{4\Omega V}, \quad (64)$$

we are led to the following simple relation between P and ΔP :

$$\frac{1}{\Delta P} - \frac{1}{\Pi_0} \simeq \frac{\sigma/\pi}{(P - P_* + \sigma/\sqrt{3})^2 + \sigma^2}. \quad (65)$$

The right hand of equation (65) is a Lorentzian function. This indicates

$$\int_{-\infty}^{\infty} \left(\frac{1}{\Delta P} - \frac{1}{\Pi_0} \right) dP = 1, \quad (66)$$

which corresponds to the continuity limit of equation (3).

If the control parameter σ , which is proportional to ϵ , is larger, the width and the height of the Lorentzian function are larger and lower,

³ In the exceptional case of $s_1 > s_* > s_2$, s_1 and s_2 belong to the same branch of the cotangent function. We can however obtain the same equation as equation (63) even in this case by considering the reciprocal of the cotangent function (namely, the tangent function), for which s_1 and s_2 are on the two different adjacent branches.

respectively. Equation (65) implies that the dip structure in the P – ΔP relation can also be described by the (unnormalised) Lorentzian function as

$$\Delta P \simeq \Pi_0 \left(1 - \frac{\Pi_0 \sigma / \pi}{(P - P_* + \sigma / \sqrt{3})^2 + \sigma^2 + \Pi_0 \sigma / \pi} \right). \quad (67)$$

We reemphasize that equations (65) and (67) are expressions in the co-rotating frame of reference. We can easily show that the width and the depth of the dip are larger and shallower, respectively, for larger σ (ϵ).

It should also be noted that the Lorentzian function on the right-hand side of equation (65) (or equation 67) takes its maximum (minimum) not at $P = P_*$, but at $P = P_* - \sigma / \sqrt{3}$. Accordingly, the period-spacing ΔP is the smallest at a period slightly shorter than P_* , which corresponds to the period of the pure inertial mode.

In Fig. 5, we compare the solutions of equation (57) with the profiles computed by equation (67). We generally find good agreement up to the order of ϵ . In fact, the small differences for $\sigma = 4.0$ hrs are of the order of ϵ^2 .

3.4 The case of non-Uniform density core

We show in this section that the analyses developed in Sections 3.2 and 3.3 can be generalised to the more realistic case in which the density of the convective core is not uniform.

For this purpose, we formally replace equations (45) and (46) with

$$\frac{\xi_{r,\text{con}}}{R_{\text{core}}} \Big|_{r=R_{\text{core}}} = \sum_{\ell} g_{\ell}(s) \tilde{P}_{\ell}^m(\mu) \quad (68)$$

and

$$\frac{p'_{\text{con}}}{p\Gamma_1} \Big|_{r=R_{\text{core}}} = \frac{\omega^2 R_{\text{core}}^2}{c_s^2} \sum_{\ell} h_{\ell}(s) \tilde{P}_{\ell}^m(\mu), \quad (69)$$

respectively, in which g_{ℓ} and h_{ℓ} can be regarded as the coefficients of the Legendre expansion of $\xi_{r,\text{con}}$ and p'_{con} at $r = R_{\text{core}}$, respectively.

Accordingly, we obtain instead of equations (48) and (49)

$$\sum_k a_k \epsilon X_k(s) \Theta_k^m(\mu; s) = \sum_j b_j \sum_{\ell} g_{j,\ell}(s) \tilde{P}_{\ell}^m(\mu) \quad (70)$$

and

$$\sum_k a_k Y_k(s) \Theta_k^m(\mu; s) = \sum_j b_j \sum_{\ell} h_{j,\ell}(s) \tilde{P}_{\ell}^m(\mu), \quad (71)$$

respectively, where the suffix j represents the index of pure inertial modes. Similarly to the analysis in Section 3.2, we can obtain the expression that corresponds to equation (57) as

$$\tilde{F}(s) \frac{\sqrt{3} \alpha s^{2/3}}{2 \lambda^{2/3}} \left[\cot\left(\frac{\pi^2 s}{\Omega \Pi_0} - \frac{\pi}{6}\right) + \frac{1}{\sqrt{3}} \right] \simeq \epsilon, \quad (72)$$

where $F(s)$ in equation (57) has been replaced by

$$\tilde{F}(s) \equiv - \left(\sum_{\ell'} c_{k,\ell'} g_{j,\ell'}(s) \right) \left(\sum_{\ell''} c_{k,\ell''} h_{j,\ell''}(s) \right)^{-1}. \quad (73)$$

We are therefore led to equation (65) again with F replaced by \tilde{F} in equation (61). Note that we cannot generally write down the analytical expressions of \tilde{F} and its zero point s_* , both of which depend on the structure of the convective core.

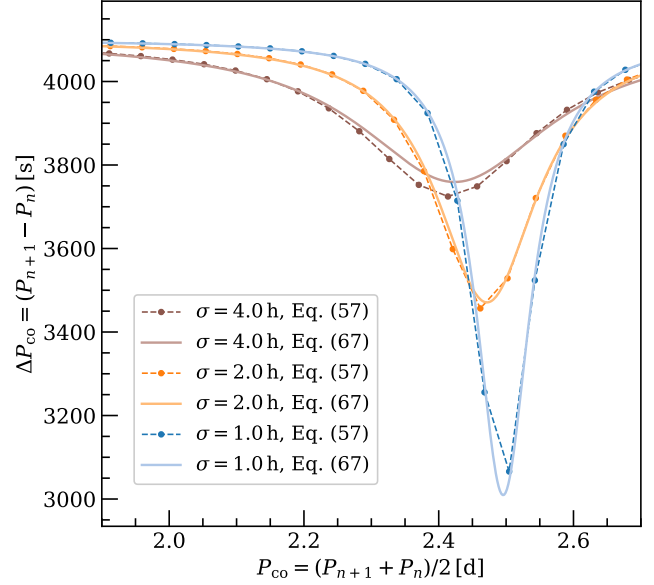


Figure 5. P – ΔP diagram (in the co-rotating frame) with the solutions of equation (57) (filled circles connected with dashed lines) and the profiles given by equation (67) (solid lines) for $2\pi/\Omega = 0.445$ d, $\Pi_0 = 4100$ s and $\sigma = 1.0, 2.0$ and 4.0 h, which correspond to $\epsilon = 6.43 \times 10^{-3}, 1.29 \times 10^{-2}$ and 2.57×10^{-2} , respectively. We adopt equation (59) for $F(s)$. Note that P_n indicates the n -th shortest period and that the abscissa means the average period of two neighbouring solutions, $P = (P_n + P_{n+1})/2$.

3.5 The case of non-Uniform and discontinuous density profile

We have so far assumed that both ρ and $d\rho/dr$ are continuous near the core boundary. However, the numerical calculations suggest it more appropriate to regard that the density is discontinuous or indifferentiable near the boundary (see Appendix B). We therefore present the analysis for such discontinuous cases in this section. We suppose that the discontinuous point of the density profile is located at $r = R_{\text{core}}$ and that the left-hand and right-hand limits of the density are defined as

$$\lim_{r \rightarrow R_{\text{core}}-0} \rho = \rho_b \quad (74)$$

and

$$\lim_{r \rightarrow R_{\text{core}}+0} \rho = \rho_b + \Delta\rho, \quad (75)$$

respectively. Note that $\Delta\rho$ is usually negative.

Accordingly, the discontinuity in N near the boundary is generally described as

$$\lim_{r \rightarrow R_{\text{core}}-0} N = 0, \quad (76)$$

$$N|_{r=R_{\text{core}}} = \infty \quad (77)$$

and

$$\lim_{r \rightarrow R_{\text{core}}+0} N = N_0. \quad (78)$$

The numerical results actually demonstrate two different kinds of discontinuous cases. In case (1), the density is continuous while its derivative is not. On the other hand, both the density and its derivative are discontinuous in case (2). In above equations (74)–(75) and (76)–(78), the cases (1) and (2) can be specified by setting $\Delta\rho = 0$ and

$\Delta\rho \neq 0$, respectively. In addition, equation (77) is not relevant for case (1).

As in Section 3.2, the eigenvalue conditions can be obtained by matching ξ_r and δp at the boundary between the core and envelope. While we may basically follow the same method as in Section 3.1.1 to construct the envelope solutions, we can replace the Airy functions with their asymptotic forms because k_r remains to be large even near the inner boundary of the propagative cavity, which coincides with the discontinuous point. With $d = 0$, equations (13) and (14) can be rewritten into

$$v \simeq -\frac{c}{\sqrt{\pi}} \frac{1}{\sqrt{k_r}} \sin\left(\int_r^{r_b} k_r dr - \frac{\pi}{4}\right) \quad (79)$$

and

$$w \simeq \frac{c}{\sqrt{\pi}} \frac{1}{\sqrt{k_r}} \cos\left(\int_r^{r_b} k_r dr - \frac{\pi}{4}\right), \quad (80)$$

respectively, and then, from equation (8) and (9), we obtain

$$\lim_{r \rightarrow R_{\text{core}+0}} \frac{\xi_{r,\text{rad}}}{r} = \sum_k a_k \tilde{\epsilon} \tilde{X}_k(s) \Theta_k^m(\mu; s) \quad (81)$$

and

$$\lim_{r \rightarrow R_{\text{core}+0}} \frac{p'_{\text{rad}}}{p\Gamma_1} = \frac{\omega^2 R_{\text{core}}^2}{c_s^2} \sum_k a_k \tilde{Y}_k(s) \Theta_k^m(\mu; s), \quad (82)$$

where

$$\tilde{X}_k(s) \equiv 2\lambda^{1/4} s^{1/2} \sin\left(\frac{\pi^2 s}{\Omega\Pi_0} - \frac{\pi}{4}\right) \quad (83)$$

and

$$\tilde{Y}_k(s) \equiv -\lambda^{-1/4} s^{3/2} \cos\left(\frac{\pi^2 s}{\Omega\Pi_0} - \frac{\pi}{4}\right). \quad (84)$$

Note that the parameter $\tilde{\epsilon}$ is defined as

$$\tilde{\epsilon} \equiv \frac{\Omega}{N_0}. \quad (85)$$

On the other hand, the core solutions are the same as equations (68) and (69).

Using equations (68) and (81), we obtain the matching condition of ξ_r as

$$\sum_k a_k \tilde{\epsilon} \tilde{X}_k(s) \Theta_k^m(\mu; s) = \sum_j b_j \sum_\ell g_{j,\ell}(s) \tilde{P}_\ell^m(\mu). \quad (86)$$

Similarly, from equations (69), (82) and (86), we can derive the condition of $\delta p = p' + \xi_r(\partial p/\partial r)$ as

$$\begin{aligned} \sum_k a_k \left(1 + \frac{\Delta\rho}{\rho_b}\right) \left[\tilde{Y}_k(s) - \frac{GM_{\text{core}}}{\omega^2 R_{\text{core}}^3} \tilde{\epsilon} \tilde{X}_k(s) \right] \Theta_k^m(\mu; s) \\ = \sum_j b_j \left[\sum_\ell h_\ell(s) - \frac{GM_{\text{core}}}{\omega^2 R_{\text{core}}^3} \sum_\ell g_{j,\ell}(s) \right] \tilde{P}_\ell^m(\mu). \end{aligned} \quad (87)$$

With the same assumptions as those in Section 3.2, we can reduce these matching conditions to

$$\cot\left(\frac{\pi^2 s}{\Omega\Pi_0} - \frac{\pi}{4}\right) + \tilde{\epsilon} \frac{GM_{\text{core}}}{\omega^2 R_{\text{core}}^3} \frac{\Delta\rho}{\rho_b + \Delta\rho} \frac{2\lambda^{1/2}}{s} \Big|_{s=s^*} \simeq -\frac{\tilde{\epsilon}/\tilde{V}}{(s-s^*)}, \quad (88)$$

where

$$\tilde{V} \equiv -\left(1 + \frac{\Delta\rho}{\rho_b}\right) \left[\frac{d\tilde{F}(s)}{ds} \frac{s}{2\lambda^{1/2}} \right]_{s=s^*}. \quad (89)$$

Note that $\tilde{F}(s)$ is the same as equation (73). Equation (88) can approximately be solved for the period-spacing ΔP to yield

$$\frac{1}{\Delta P} - \frac{1}{\Pi_0} \simeq \frac{\tilde{\sigma}/\pi}{(P - P_*)^2 + \tilde{\sigma}^2}, \quad (90)$$

where

$$\tilde{\sigma} \equiv \frac{\pi\tilde{\epsilon}}{\Omega\tilde{V}}. \quad (91)$$

Comparing equation (90) for the discontinuous N^2 profiles with equation (65) for the continuous profiles, we find the following points: (1) the inverse of the period-spacing $1/\Delta P$ is essentially described by the normalised Lorentzian functions of the period P in the both cases; (2) the width (σ) of the Lorentzian profiles depends on the structure of N^2 near the interface through ϵ (cf. equation 23) and the property of the core inertial oscillation through V (cf. equation 61) for the continuous case, while they are replaced by $\tilde{\epsilon}$ (cf. equation 85) and \tilde{V} (cf. equation 89), respectively, for the discontinuous case; (3) the central position of the Lorentzian profiles is located at the period of the core inertial mode (P_*) for the discontinuous case, whereas it is offset by $-\sigma/\sqrt{3}$ for the continuous case. It should also be noted that the formal limit of $dN^2/dr \rightarrow \infty$ ($\epsilon \rightarrow 0$) in the continuous case corresponds to the discontinuous case with $N_0 \rightarrow \infty$ ($\tilde{\epsilon} \rightarrow 0$). In this limit, there is no interaction of oscillations between the convective core and the radiative envelope.

4 COMPARISON WITH NUMERICAL SOLUTIONS

In this section, we compare the analyses developed in Section 3 with the results of numerical calculations in two respects. We first check the main conclusion that the dip structure is described by the Lorentzian profile in Section 4.1 based on the results by Saio et al. (2021). We then study the evolution of the main parameter $\tilde{\epsilon}$ that controls the dip structure in Section 4.2 based on the MESA stellar evolution code (Paxton et al. 2011, 2013, 2015, 2018, 2019).

4.1 Fitting the Lorentzian functions

According to equation (65) or (90), the inverse of the period-spacing $1/\Delta P$ is described by the Lorentzian function. We check how accurate this description is based on the numerical results given in Fig. 4 of Saio et al. (2021), which are supplemented by one more case with the central hydrogen mass fraction (X_c) of 0.06. By carefully examining N^2 of the equilibrium models, we adopt equation (90) for the discontinuous profiles to interpret the fitted parameters of the Lorentzian functions.

When we analyse the numerical results, we should note that there are two points that are not considered in deriving equation (90). As we see in Fig. 4 of Saio et al. (2021), the period-spacing ΔP can have a significant wavy component, which is generally caused by rapid change in the equilibrium structure (e.g. Miglio et al. 2008). In addition, while we assume that Π_0 is constant as a function of the period P , this is not completely supported by the numerical results of Saio et al. (2021), because the profiles of ΔP outside the dips are inclined. Taking these points into account, we fit $1/\Delta P$ with function $f(P)$ defined as

$$f(P) = x_1 - x_2 P + \frac{\tilde{\sigma}/\pi}{(P - P_*)^2 + \tilde{\sigma}^2}, \quad (92)$$

where x_1 and x_2 (as well as $\tilde{\sigma}$ and P_*) are the constant parameters to be fitted. Comparing $f(P)$ with equation (90), we find that $(\Pi_0^*)^{-1} \equiv$

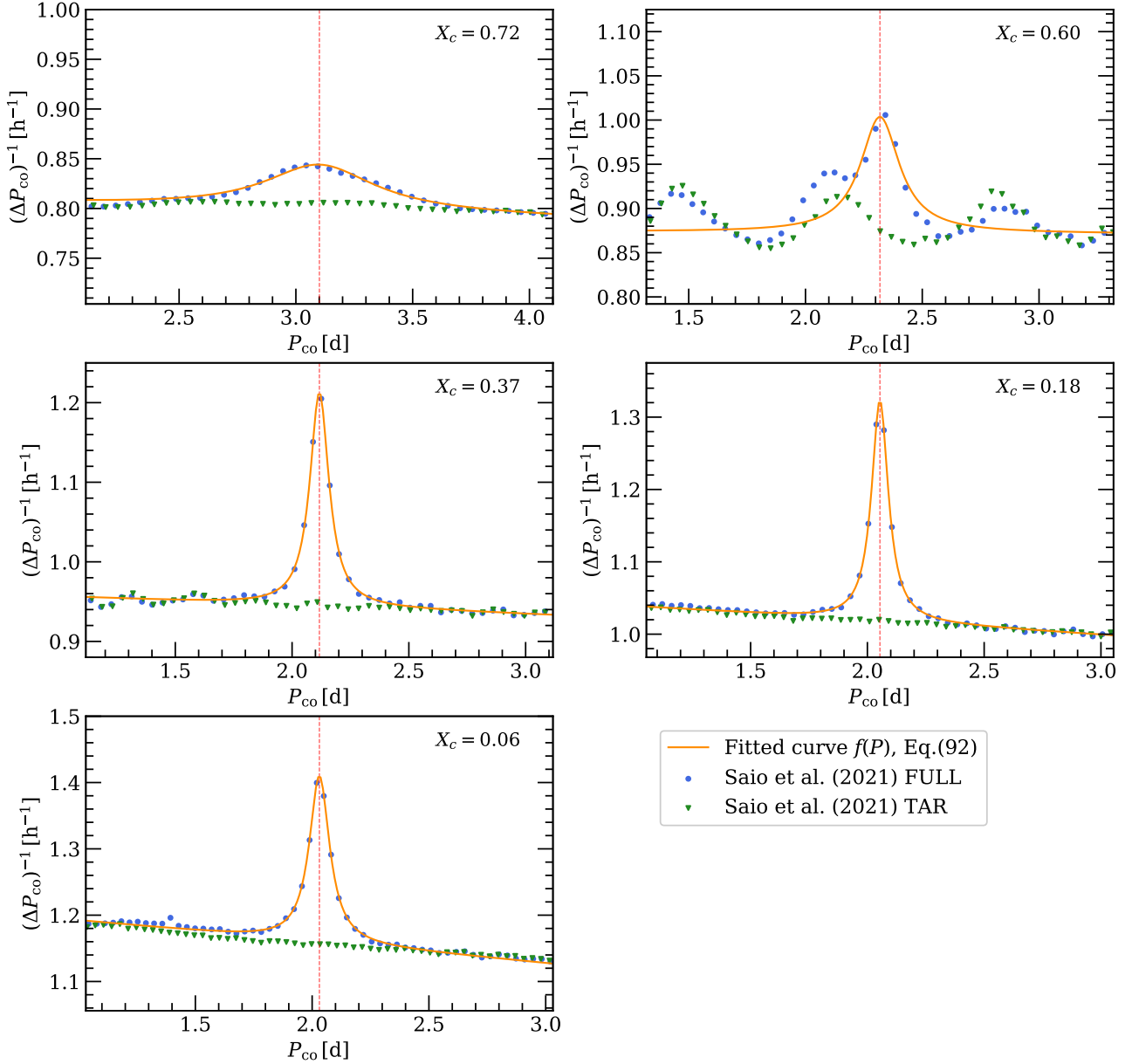


Figure 6. $P-1/\Delta P$ diagram (in the co-rotating frame) constructed from the numerical results used in Fig. 4 of Saio et al. (2021) with an additional case with the central hydrogen mass fraction of 0.06 (blue filled circles mean those of full calculation, while green triangles indicate those under the traditional approximation of rotation) and fitted curves by function $f(P)$, which is given by equation (92) (orange lines). The stellar mass and rotation period are set to $1.5 M_{\odot}$ and 0.455 d, respectively. In each panel, X_c is the hydrogen mass fraction at the centre, which monotonically decreases with the evolution. The red vertical dashed lines represent the peak position of the Lorentzian function, P_* .

Table 1. Fitting parameters x_1 , x_2 , $\bar{\sigma}$ and P_* obtained by the least-squares method in Fig. 6 and $\bar{\epsilon}$ calculated based on the evolutionary stellar models used in Fig. 4 of Saio et al. (2021).

X_c	x_1 [h^{-1}]	x_2 [10^{-3}h^{-2}]	$(\Pi_0^*)^{-1}$ [h^{-1}]	$\bar{\sigma}$ [h]	P_* [d]	$\bar{\epsilon}$
0.72	0.820 ± 0.001	0.292 ± 0.011	0.798 ± 0.002	6.906 ± 0.194	3.101 ± 0.008	0.343
0.60	0.875 ± 0.011	0.048 ± 0.316	0.873 ± 0.029	2.428 ± 0.184	2.319 ± 0.007	0.037
0.37	0.968 ± 0.002	0.465 ± 0.032	0.944 ± 0.003	1.183 ± 0.013	2.117 ± 0.001	0.018
0.18	1.058 ± 0.001	0.825 ± 0.024	1.018 ± 0.003	1.040 ± 0.009	2.054 ± 0.000	0.018
0.06	1.224 ± 0.002	1.348 ± 0.041	1.159 ± 0.004	1.264 ± 0.009	2.031 ± 0.000	0.020

$x_1 - x_2 P_*$ provides an estimate of Π_0^{-1} in the period range that includes the dip. Fig 6 and Table 1 present the results of the fitting, which are computed by the fit function of `GNUPLLOT`.

We observe in Fig. 6 that the numerical results (blue filled circles) are fitted by the Lorentzian functions (orange lines) quite well except in the case of $X_c = 0.60$, in which the contribution of the wavy component is significant in the numerical results. In fact, we find from Table 1 that the relative uncertainties in $\tilde{\sigma}$ are 8 per cent for $X_c = 0.60$ and less than 3 per cent for the other cases.

According to Table 1, $\tilde{\sigma}$ first decreases rapidly along with the evolution until $X_c = 0.37$ (from 6.9 h for $X_c = 0.72$ to 1.2 h for $X_c = 0.37$). The initial decrease in $\tilde{\sigma}$ is associated with growth of the convective core (cf. Fig. B1). Then, the decrease becomes milder between $X_c = 0.37$ and $X_c = 0.18$. Finally, $\tilde{\sigma}$ turns to increase slightly from 1.0 h for $X_c = 0.18$ to 1.3 h for $X_c = 0.06$. The peak position P_* monotonically gets smaller along with the evolution, though it changes less rapidly than $\tilde{\sigma}$ between 3.0 d for $X_c = 0.72$ and 2.1 d for $X_c = 0.37$. On the other hand, the monotonic decrease in Π_0^* is caused by the increase of the maximum value of N^2 , which is realised just outside the convective core.

4.2 Evolution of $\tilde{\epsilon}$

In Section 3, we have shown that ϵ (or $\tilde{\epsilon}$), which is defined as equation (23) (or equation 85), is the fundamental parameter that controls the strength of the interaction between the pure inertial waves in the convective core and the gravito-inertial waves in the radiative envelope. Moreover, it has a direct influence on the width and depth of the dip structure in the period-spacing. We numerically estimate this parameter in this section. The details of the parameter settings of MESA are given in Appendix B.

The top panels of Fig. 7 present the evolution of $\tilde{\epsilon}$ during the main-sequence stage as functions of the central hydrogen mass fraction (X_c) for the models with 1.4, 1.5, 1.6 and 1.8 M_\odot , whereas the bottom panels show the corresponding evolution of the mass of the convective core (M_{core}). The blue (orange) lines represent the results obtained by adopting the Ledoux (Schwarzschild) criterion for convection (cf. Appendix B). Ignoring jaggy structures, which probably reflect numerical errors, we commonly observe for the three values of mass that, along with the evolution (from right to left in the figure), $\tilde{\epsilon}$ first decreases steeply in the early phase, takes its minimum at an intermediate stage, and then comes to increase very slowly in the later phase. On the other hand, M_{core} shows the opposite behaviour. It increases first and turns to decrease after taking its maximum near the stage when $\tilde{\epsilon}$ gets minimum.

The negative correlation between $\tilde{\epsilon}$ and M_{core} can readily be understood. We first note that the right-hand side limit N_0 is mostly determined by the gradient of the mean molecular weight in the mass coordinate. As M_{core} increases in the early phase, the gradient becomes larger near the inner boundary of the radiative envelope (cf. Fig. B1). When the core starts to shrink, the steep gradient that is created during the growing phase and left behind in the radiative core is quickly smoothed out because of the element diffusion. In the later phase of core shrinkage, the gradient of the mean molecular weight on the radiative side of the boundary gets milder because the core shrinkage rate $|dM_{\text{core}}/dX_c|$ increases.

Turning to the difference between the Ledoux and Schwarzschild cases, we find in Fig. 7 that, for all of the masses, $\tilde{\epsilon}$ is slightly larger in the Ledoux case than in the Schwarzschild case during the core growth except for the very early stage, though M_{core} has little difference between the two cases for the all values of X_c . As explained in Paxton et al. (2019), the convective premixing effectively reproduces

semiconvection, which induces slow mixing in a shallow layer just outside the convective core so that the radiative temperature gradient is equal to the adiabatic value. While the both cases take this process into account, the resultant structure depends on which convective criterion is adopted.⁴ The larger $\tilde{\epsilon}$ for the Ledoux case is caused by smaller N^2 in the layer, which is realised by smoother abundance profiles. It is actually still a matter of debate how we should formulate mixing processes at the boundary between the convective core and the radiative envelope. While we do not intend to give the final answer to this problem in this paper, Fig. 7 clearly shows that the two different cases can be discriminated by measuring $\tilde{\epsilon}$ in the core growing phase of evolution. This particular example demonstrates potential of $\tilde{\epsilon}$ as a diagnostic parameter in asteroseismology.

In the last column of Table 1, we present $\tilde{\epsilon}$ of the models in Fig. 4 of Saio et al. (2021). Comparing the evolutionary change in $\tilde{\epsilon}$ with that in $\tilde{\sigma}$, we find that the both parameters follow the similar trend. They decrease rapidly from $X_c = 0.72$ to 0.60 by factors 3.0 and 9.3 for $\tilde{\sigma}$ and $\tilde{\epsilon}$, respectively, and then mildly from $X_c = 0.60$ to 0.37 with nearly the same factor of ~ 2 . Then, they show little variation between $X_c = 0.37$ and 0.18 with -10 and $+3$ per cent decrease in $\tilde{\sigma}$ and $\tilde{\epsilon}$, respectively. Finally, they both show increase between $X_c = 0.18$ and 0.06 by $+21$ and $+11$ per cent in $\tilde{\sigma}$ and $\tilde{\epsilon}$, respectively. We therefore understand that, except for the initial phase when the convective core grows rapidly (cf. Fig. 7), the change in $\tilde{\sigma}$ is mainly controlled by that in $\tilde{\epsilon}$, which implies that \tilde{V} does not change significantly (cf. equation 91).

5 DISCUSSION

5.1 Asteroseismology of the dip

We have analysed how the dip structure in the P - ΔP diagram is formed as a result of the interaction between pure inertial waves in the convective core and gravito-inertial waves in the radiative envelope (forward problem). Once we understand the physics of the dip formation, we may ask what kind of structure information we can derive from the dip (inverse problem). We find that the corresponding hump structure in the P - $1/\Delta P$ diagram is approximately described by a normalised Lorentzian function. While we consider two cases, those of continuous and discontinuous profiles, they agree in the functional form of the hump structure, which is given by equations (65) and (90), respectively. For simplicity, we base our discussion in this section on equation (90) for the case of discontinuous profiles.

Because $\tilde{\sigma}$ is essentially the ratio between $\tilde{\epsilon}/\tilde{V}$ and Ω (the rotation rate of the radiative envelope) (cf. equations 89 and 91), and Ω can be estimated independently from the frequency spectrum outside the dip, we may regard P_* (the period of the pure inertial mode in the core) and $\tilde{\epsilon}/\tilde{V}$ as two structural parameters that we can derive from the dip (or hump). Strictly speaking, we cannot determine $\tilde{\epsilon}$ and \tilde{V} separately without any additional assumptions. In fact, although function \tilde{F} , on which \tilde{V} depends (cf. equation 89), is explicitly given by equation (58) in the case of uniform-density cores, it generally depends on the core structure through g_ℓ and h_ℓ (cf. equation 73). However, since the evolutionary change in $\tilde{\sigma}$ largely depends on that in $\tilde{\epsilon}$ (cf. discussion at the end of Section 4.2), we may estimate the

⁴ In the models we construct, the boundary condition that the radiative and adiabatic temperature gradients are equal to each other on the convective side of the boundary (e.g. Gabriel et al. 2014) is more accurately satisfied in the Schwarzschild case than in the Ledoux case.

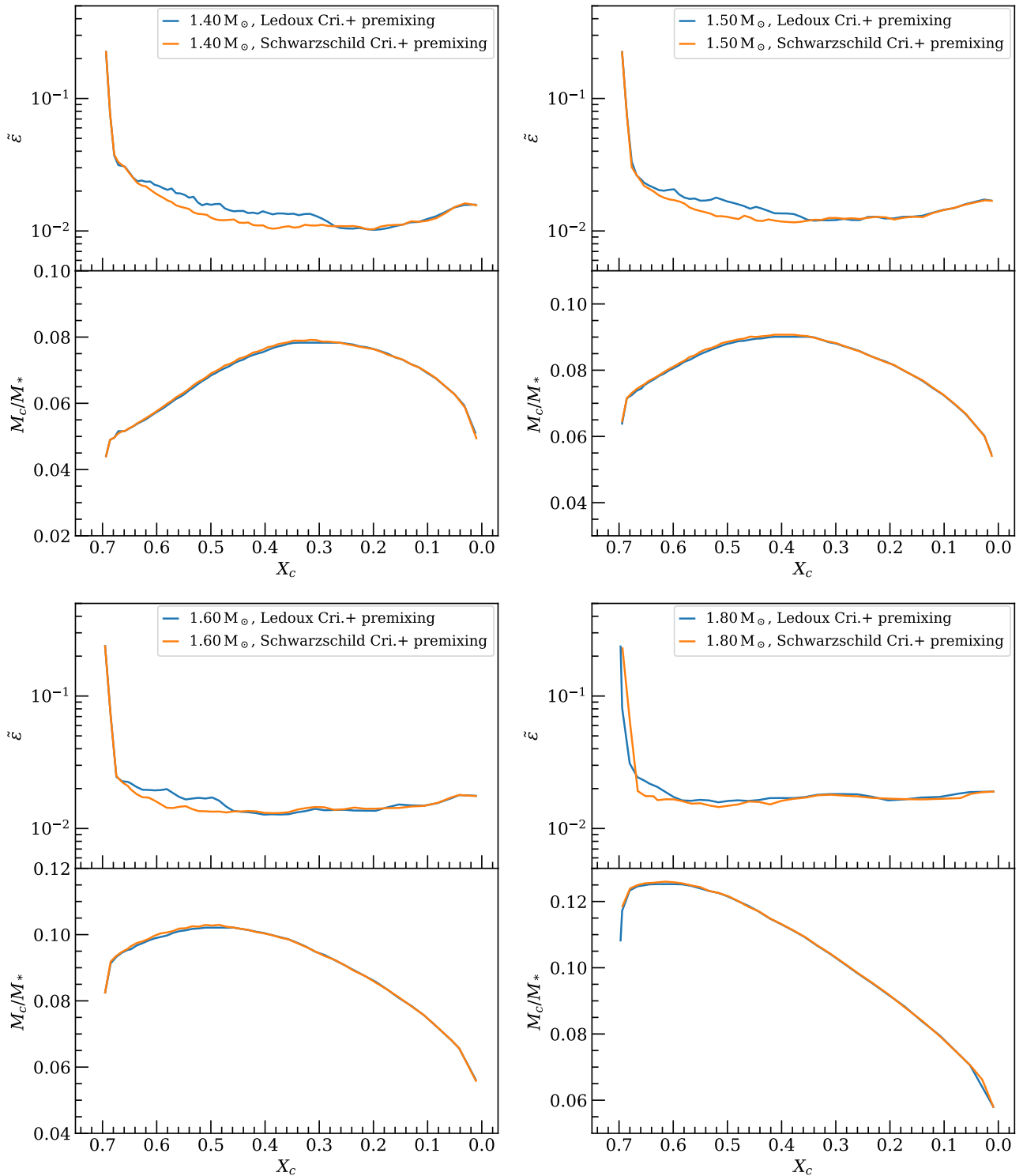


Figure 7. Evolution of ϵ and M_{core} as function of the central hydrogen mass fraction X_c for the models with 1.4 (upper left panels), 1.5 (upper right panels), 1.6 (lower left panels) and $1.8 M_{\odot}$ (lower right panels). The ordinates represent ϵ (upper panels) and M_{core} (lower panels). The core mass M_{core} is normalised by the total stellar mass M_* . Note that X_c decreases during the evolution from 0.70 at the zero-age main-sequence stage. The blue and orange lines correspond to the Ledoux and Schwarzschild cases, respectively (refer to Appendix B for the details). We set the rotation period to 0.455 d for all the cases.

relative change in the Brunt–Väisälä frequency in the boundary layers from that in the dip structure.

As we have discussed in Section 4.2, since we do not understand the mixing process in stars completely, there exist uncertainties in the estimate of $\tilde{\epsilon}$ in the forward problem based on the evolutionary models. On the other hand, if the observed frequencies are precise enough, we may measure the shape of the dips so accurately that we can estimate $\tilde{\epsilon}/\tilde{V}$ reliably. In this sense, the inverse problem could be more useful than the forward problem to probe the structure at the boundary between the convective core and the radiative envelope of γ Dor stars.

5.2 Roles of the geometric property

Ouazzani et al. (2020) suggest that the resonance between a pure inertial mode in the core and a gravito-inertial mode in the envelope could mainly be controlled by the geometric factor, which measures how close their angular structures are to each other. In the case of the uniform-density core, this factor is simply given in our formulation by $c_{k,\ell}$ that is defined by equation (53) (provided that the Hough function Θ_k^m is properly normalised). Ouazzani et al. (2020) regard that the interaction between the core and envelope modes with larger values of $c_{k,\ell}$ leads to stronger resonance, which corresponds to wider and shallower dips in the P – ΔP diagram. On the other hand, the analysis in the present paper demonstrates that the width (as well as the depth) of the dips is essentially fixed by $\tilde{\sigma}$, which is determined by $\tilde{\epsilon}/\tilde{V}$ and Ω (the rotation rate of the envelope). We actually consider $\tilde{\epsilon}$ as the most important parameter of the interaction, though it is not related to the geometrical factor, but is essentially controlled by the chemical composition profiles near the boundary between the core and the envelope. Still, we admit that the geometric factor is also important in our formulation in two respects. The first point is found when we approximate the matching condition of equation (54) by equation (56). In this approximation, we replace the determinant of an infinite matrix by the most dominant element. For this to be valid, we have to assume that the geometry factor, $c_{k,\ell}$, which is a common factor of the terms in the most dominant element, is not negligibly small. On the other hand, we observe the second point in equation (73). The numerator and denominator of the right-hand side of this equation are essentially equal to the integrals of $\xi_{r,\text{con}}\Theta_k^m$ and $p'_{\text{con}}\Theta_k^m$, respectively, over the sphere at $r = R_{\text{core}}$. They therefore provide measures of how close the angular structures of $\xi_{r,\text{con}}$ and p'_{con} are to Θ_k^m at the outer boundary of the convective core. Since V depends on the ratio of these measures (cf. equation 61), the width and the depth of the dip structure, which are controlled by $\tilde{\epsilon}/\tilde{V}$ cannot simply be determined by the angular structure of either $\xi_{r,\text{con}}$ or p'_{con} .

5.3 Impact of the convective overshooting

Saio et al. (2021) examined how the convective overshooting influences the dip structure in the $\nu_{\text{co-rot}}-\Delta P_{\text{co-rot}}$ diagram. Taking the diffusive overshooting (Herwig 2000) into account, they showed that a single (isolated) dip structure in the case of no convective overshooting turns into multiple dips. We reconsider here this phenomenon based on the picture presented in this paper. More specifically, we rely on the analysis for continuous profiles in Section 3.3 because the overshooting causes additional mixing. As Saio et al. (2021) demonstrate in their Figs. 8 and 9, the diffusive convective overshooting generates a thin intermediate radiative layer between the convective core and the steep chemical composition gradient layer in the radiative envelope. There thus exist three separate regions of wave

propagation. However, because the constant period-spacing (outside the dip structure) comes from the propagation in the radiative region above the steep chemical composition gradient, we may treat the inner two regions (the convective core and the intermediate radiative zone) together to discuss the formation of the dip structure. In order to understand the relation between the dips and the wave propagation, we pay attention to the case of $M = 1.50 M_{\odot}$, $f_{\text{ov}} = 0.02^5$ (the larger overshooting parameter) and $X_c = 0.06$, in which three dips appear around 0.23 d^{-1} , 0.31 d^{-1} and 0.40 d^{-1} in the $\nu_{\text{co-rot}}-\Delta P_{\text{co-rot}}$ diagram (cf. green filled circles in the upper right panel of Fig. 7 of Saio et al. 2021). Observing the profiles of the corresponding radial displacement ξ_r around the centre of each dip in the right panel of their Fig. 9, we find that the number of nodes increases one by one in the inner two layers as $\nu_{\text{co-rot}}$ decreases, though they are located only in the intermediate radiative layer and the upper part of the convective core. Based on this observation, we speculate that, due to the appearance of the intermediate radiative layer, where gravito-inertial waves can propagate, a pure inertial mode in the convective core is split into multiple eigenmodes in the inner two regions, and that each of the split modes interacts with the gravito-inertial modes in the outer radiative region above the steep chemical composition gradient to produce a dip in the P – ΔP (or $\nu_{\text{co-rot}}-\Delta P$) diagram based on the mechanism that we propose in Section 2. We therefore expect to find more dips (with more nodes of the corresponding ξ_r) in the diagram if we extend the diagram to the lower-frequency (longer-period) range than are shown in Saio et al. (2021). As they discuss, if the overshooting does not create the intermediate radiative layer but just extends the convective core as in the case of convective penetration (Zahn 2002), the number of dips in the P – ΔP diagram does not change. Therefore, we may get information about the overshooting process by checking whether the dip is split or not. Saio et al. (2021) also point out that the width and depth of dips in the case of overshooting are broader and shallower, respectively, which implies that the interaction gets stronger, than in the case without overshooting. In this case, we may consider the interaction of waves between the two inner regions (the convective core and the intermediate radiative region). Because the shape of the dips are controlled by ϵ/V (see Section 3), we may interpret that the shape change is because of the increase in ϵ , which is in turn caused by the shallower gradient of N^2 in the intermediate radiative region. Figs. 8 and 9 of Saio et al. (2021) are consistent with this interpretation.

5.4 Frequency dependence of period-spacing

In Section 3, we assumed that the period-spacing of the gravito-inertial mode Π_0 is constant irrespective of period P (or the spin parameter s) for simplicity. However, the numerical results given in Fig. 4 of Saio et al. (2021) suggest that $1/\Delta P$ (or ΔP) generally decreases (or increases) with P . To take this property into account, we adopted linear function $x_1 - x_2 P$ for fitting the base line of the hump structure in $1/\Delta P$ in Section 4.1. We discuss here the cause of this tendency. It should be noted that, in this section, ΔP represents the period-spacing with the frequency dependence, and that Π_0 means the constant period-spacing in the limit of an infinite period (cf. equation 21).

We can give three possible ideas for explaining the frequency dependence of ΔP . The first one is lack of resolution in the numerical calculations, which results in the wavelengths of oscillations comparable to (or even smaller than) the mesh sizes of equilibrium models.

⁵ Saio et al. (2021) use h_{os} for f_{ov} .

Saio et al. (2021) point out that this is the reason for the increase in the period-spacings particularly in the low frequency (large s) limit, for which the radial wavelengths are extremely short. The second idea is low accuracy of the asymptotic formula of Π_0 given by equation (21). In fact, we demonstrate in Appendix A that the formula can be corrected to explain the non-constant period-spacings. The third idea is the wavy component caused by rapid change in the equilibrium structure (see Fig. 6, especially the case of $X_c = 0.60$). This component is not taken into account in the asymptotic analysis in Appendix A.

In order to examine which of the three reasons are more important in the frequency range in which the dip structure appears, we perform two additional analyses. We first compute the period-spacings under TAR for the same evolutionary models constructed by Saio et al. (2021), but with increased spatial resolution by interpolation. We call ΔP obtained by this analysis as $\Delta P_{\text{TAR IR}}$. We secondly calculate the frequencies by solving the following asymptotic condition directly:

$$\int_{r_a}^{r_b} k_r dr = (n + \hat{\alpha})\pi, \quad (93)$$

in which we assume $\hat{\alpha} = 0$ for simplicity. We refer to ΔP computed by this method as ΔP_{ASYMP} . We note that equation (21) can be derived from equation (93) for low frequencies.

We confirm in the frequency range between 0.2 and 1 d^{-1} that ΔP by Saio et al. (2021) generally agrees with $\Delta P_{\text{TAR IR}}$ in the high frequency range, whereas the former gets larger than the latter as the frequency becomes lower. This difference, which is caused by the numerical errors, tends to increase for smaller X_c . In fact, it is about 0.3 (5) per cent for $X_c = 0.72$ (0.18) at 0.2 d^{-1} . We also find in the same frequency range that ΔP_{ASYMP} can be reproduced by the corrected asymptotic formula of equation (A14) in Appendix A nearly completely. In addition, we understand that ΔP_{ASYMP} almost converges on $\Delta P_{\text{TAR IR}}$ in the low frequency limit as expected, and that both of them slightly decrease for higher frequencies. Their discrepancy in the high frequency range can be interpreted as the contributions of the wavy component and the inaccuracy of the asymptotic description.

Based on these considerations, we draw the following conclusions: the slopes of the baseline for $X_c = 0.72$ and 0.60 in Fig. 6 can mostly be explained by the corrected asymptotic formula of ΔP and the wavy component, whereas those for $X_c = 0.37$ and 0.18 have non-negligible influences of the resolution problem. However, in any case, the variation in the period-spacing is small enough in the frequency range of each dip to be approximated by a linear function, as we assume in Section 4.1.

One message in this section is that the approximation of constant period-spacing, which is widely assumed in the analysis of γ Dor stars, may not be accurate enough. This is particularly the case when we analyse the observed frequencies with very high precision, as those provided by *Kepler*. The corrected form of ΔP due to higher-order terms should be considered in such cases (cf. equation A14 or A15 in Appendix A).

5.5 Comparison with mixed modes in evolved stars

We may compare the resonantly coupled modes in γ Dor stars, which are analysed in the present paper, with mixed modes in subgiant and red giant stars (e.g. Mosser et al. 2012; Hekker et al. 2018; Appourchaux 2020). In fact, the both types of modes are constructed by the interaction between two kinds of waves with different physical characters, which are trapped in different regions of stars. In the case of γ Dor stars, the two kinds of waves are pure inertial waves in the convective core and gravito-inertial waves in the radiative envelope.

On the other hand, the mixed modes in the evolved stars are composed of gravity waves in the core and acoustic waves in the envelope.

The eigenmode condition for the mixed modes is formally given by

$$\tan \Theta_p \cot \Theta_g = q, \quad (94)$$

in which Θ_p and Θ_g are phase functions of acoustic and gravity waves, respectively. Following the dispersion relations of the waves, Θ_p and Θ_g are linear functions of the frequency and the period of oscillations, respectively. Note that equation (94) is derived in the asymptotic limit by assuming that the wavelengths of the constituent waves are much shorter than the scale height of the equilibrium structure. This assumption is accurate for red giants and in the late stage of subgiants. The left-hand side of equation (94) is a product of the core variable $\cot \Theta_g$ and the envelope variable $\tan \Theta_p$, whereas the right-hand side is the coupling factor q , which is determined by the properties of the intermediate evanescent region (cf. Unno et al. 1989; Takata 2016; Pinçon et al. 2020). In fact, we observe the same structure in equation (60). The first part of the left-hand side of this equation, $-V(s - s_*)$, depends on the properties of the pure inertial waves in the convective core, while the second part in the square bracket represents the physical character of the gravito-inertial waves in the radiative envelope. In addition, ϵ on the right-hand side is the control parameter of the interaction, which is determined by the structure of the interface between the convective core and the radiative envelope. We may therefore regard the resonantly coupled modes in γ Dor stars as another kind of mixed modes.

6 CONCLUSION

We have discussed the formation process of the dip structure in the period and period-difference diagram of γ Dor stars, which is recently found in the observations (Saio et al. 2018b) and is reproduced in the numerical calculations (Ouazzani et al. 2020; Saio et al. 2021). We have first presented a simple and qualitative picture of the dip formation that relies on the following two key processes: (1) insertion of a pure inertial mode of the convective core into the frequency spectrum of gravito-inertial modes of the radiative envelope, which exhibits equal spacing in period, and (2) relaxation of the modes in the spectrum due to the avoided crossings. Based on the picture that the dip is generated as a result of interaction between the pure inertial waves in the convective core and the gravito-inertial waves in the radiative envelope, we have formulated the problem by using approximate analytic expressions of the wave solutions in each region. We have found that the main control parameter of the interaction is ϵ (or $\bar{\epsilon}$ if the structure is discontinuous) that is inversely correlated with the variation in the squared Brunt–Väisälä frequency at the convective-core boundary. The shape of the dip can approximately be described by the Lorentzian function whose width and height depend on ϵ (or $\bar{\epsilon}$) in the sense that the width and height are broader and lower, respectively, as ϵ (or $\bar{\epsilon}$) is larger. We have also demonstrated based on the evolutionary calculations that the change of $\bar{\epsilon}$ is almost synchronised with the mass of the convective core. In particular, ϵ becomes minimum, which means that the interaction becomes minimum, when the mass of the convective core becomes maximum during the main-sequence evolution. Because the stellar structure just outside the convective core sensitively depends on various physical processes including diffusion, rotational mixing and convective overshooting, the information that we obtain from the observed dip structure would provide precious constraints on these processes, which still contain some theoretical uncertainties.

ACKNOWLEDGEMENTS

We thank Hideyuki Saio for providing the numerical data and constructive comments that helped a lot to improve this paper. We also acknowledge Umin Lee and Francois Lignières for their insightful comments about this study. TT is supported by IGPEES, WINGS Program, the University of Tokyo. MT is grateful for the financial support by JSPS KAKENHI Grant Numbers JP18K03695 and JP22K03672.

DATA AVAILABILITY

The data underlying this article will be shared on reasonable request to the corresponding author.

REFERENCES

- Aerts C., Christensen-Dalsgaard J., Kurtz D. W., 2010, *Asteroseismology*. Springer Science & Business Media
- Aizenman M., Smeyers P., Weigert A., 1977, *A&A*, **58**, 41
- Appourchaux T., 2020, *A&A*, **642**, A226
- Baglin A., et al., 2006, in 36th COSPAR Scientific Assembly.
- Ballot J., Lignières F., Prat V., Reese D. R., Rieutord M., 2012, in Shibahashi H., Takata M., Lynas-Gray A. E., eds, *Astronomical Society of the Pacific Conference Series Vol. 462, Progress in Solar/Stellar Physics with Helio- and Asteroseismology*. p. 389
- Balona L. A., Krisciunas K., Cousins A. W. J., 1994, *MNRAS*, **270**, 905
- Borucki W. J., et al., 2010, *Science*, **327**, 977
- Bryan G. H., 1889, *Philosophical Transactions of the Royal Society of London Series A*, **180**, 187
- Christophe S., Ballot J., Ouazzani R.-M., Antoci V., Salmon S. J. A. J., 2018, *A&A*, **618**, A47
- Cousins A. W. J., 1992, *The Observatory*, **112**, 53
- Eckart C., 1960, *Hydrodynamics of oceans and atmospheres*. Pergamon Press, Oxford
- Gabriel M., Noels A., Montalbán J., Miglio A., 2014, *A&A*, **569**, A63
- Hekker S., Elsworth Y., Angelou G. C., 2018, *A&A*, **610**, A80
- Herwig F., 2000, *A&A*, **360**, 952
- Kippenhahn R., Weigert A., Weiss A., 2012, *Stellar structure and evolution*. Springer Science & Business Media
- Krisciunas K., 1994, *Comments on Astrophysics*, **17**, 213
- Lee U., Saio H., 1997, *ApJ*, **491**, 839
- Li G., Van Reeth T., Bedding T. R., Murphy S. J., Antoci V., Ouazzani R.-M., Barbara N. H., 2020, *MNRAS*, **491**, 3586
- Maeder A., 2009, *Physics, Formation and Evolution of Rotating Stars*. Springer Science & Business Media
- Miglio A., Montalbán J., Noels A., Eggenberger P., 2008, *MNRAS*, **386**, 1487
- Mosser B., et al., 2012, *A&A*, **540**, A143
- Osaki Y., 1975, *PASJ*, **27**, 237
- Ouazzani R. M., Lignières F., Dupret M. A., Salmon S. J. A. J., Ballot J., Christophe S., Takata M., 2020, *A&A*, **640**, A49
- Papaloizou J., Pringle J. E., 1978, *MNRAS*, **182**, 423
- Paxton B., Bildsten L., Dotter A., Herwig F., Lesaffre P., Timmes F., 2011, *ApJS*, **192**, 3
- Paxton B., et al., 2013, *ApJS*, **208**, 4
- Paxton B., et al., 2015, *ApJS*, **220**, 15
- Paxton B., et al., 2018, *ApJS*, **234**, 34
- Paxton B., et al., 2019, *ApJS*, **243**, 10
- Pinçon C., Goupil M. J., Belkacem K., 2020, *A&A*, **634**, A68
- Ricker G. R., et al., 2014, *Transiting Exoplanet Survey Satellite (TESS)*. p. 914320
- Saio H., Kurtz D. W., Murphy S. J., Antoci V. L., Lee U., 2018a, *MNRAS*, **474**, 2774
- Saio H., Bedding T. R., Kurtz D. W., Murphy S. J., Antoci V., Shibahashi H., Li G., Takata M., 2018b, *MNRAS*, **477**, 2183

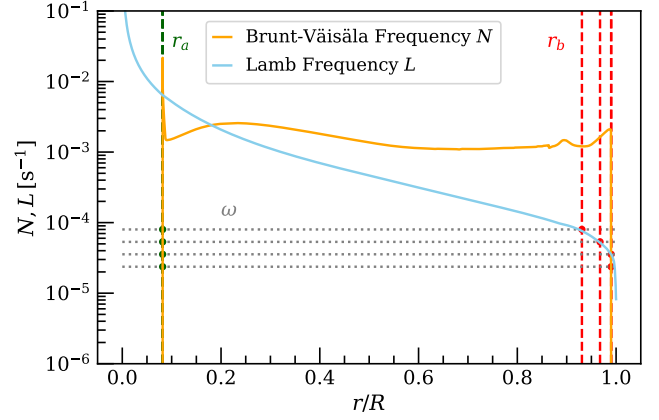


Figure A1. Typical propagation diagram of γ Dor stars in the co-rotating frame. Profiles of Brunt-Väisälä frequency N (orange solid line) and Lamb frequency L (blue solid line) are calculated by MESA. Also indicated are the locations of r_a (vertical green dashed lines) and r_b (vertical red dashed lines) for each frequency ω (horizontal gray dotted lines). Horizontal and vertical axes represent the distance from centre (normalised by the stellar radius) and the frequency, respectively. Note that we set the stellar mass $M_* = 1.5 M_\odot$, the central hydrogen mass fraction $X_c = 0.58$ and the rotation period $2\pi/\Omega = 0.455$ d.

- Saio H., Takata M., Lee U., Li G., Van Reeth T., 2021, *MNRAS*, **502**, 5856
- Takata M., 2016, *PASJ*, **68**, 109
- Takata M., Ouazzani R.-M., Saio H., Christophe S., Ballot J., Antoci V., Salmon S. J. A. J., Hijikawa K., 2020a, *A&A*, **635**, A106
- Takata M., Ouazzani R. M., Saio H., Christophe S., Ballot J., Antoci V., Salmon S. J. A. J., 2020b, *A&A*, **644**, A138
- Townsend R. H. D., 2003, *MNRAS*, **340**, 1020
- Unno W., Osaki Y., Ando H., Saio H., Shibahashi H., 1989, *Nonradial oscillations of stars*. University of Tokyo Press
- Van Reeth T., et al., 2015, *ApJS*, **218**, 27
- Van Reeth T., Tkachenko A., Aerts C., 2016, *A&A*, **593**, A120
- Wu Y., 2005, *ApJ*, **635**, 674
- Zahn J. P., 2002, in Aerts C., Bedding T. R., Christensen-Dalsgaard J., eds, *Astronomical Society of the Pacific Conference Series Vol. 259, IAU Colloq. 185: Radial and Nonradial Pulsations as Probes of Stellar Physics*. p. 58

APPENDIX A: DERIVATION OF NON-CONSTANT PERIOD-SPACING

The period-spacing of Kelvin g modes with a given azimuthal order is almost constant in the co-rotating frame in the asymptotic limit of a large spin parameter, or equivalently a low frequency (cf. equation 21). The deviation from this limit is, however, not negligible when we analyse the dip structure as in section 4.1. We therefore discuss in this section the frequency dependence of the period-spacing based on the asymptotic analysis in the traditional approximation of rotation.

We first note the frequency dependence of two parameters r_b and λ in equation (21). In Fig. A1, we depict how the inner and outer boundaries, r_a and r_b , of the propagative cavity are determined by the profiles of the Brunt-Väisälä frequency, N , and the Lamb frequency, $L = \sqrt{\lambda} c_s / r$, for a given frequency ω in a typical model of γ Dor stars. We observe that r_a is fixed by N and almost equal to the top of the convective core independently of the frequency, whereas r_b is constrained by the condition of $\omega = \min(N, L)$. As we see in the top panel of Fig. A2, r_b is nearly constant in the low frequency

range, because the condition $\omega = N$ essentially sets r_b to the base of the convective envelope. In contrast, r_b decreases almost linearly as a function of the frequency in the high frequency range, where r_b is fixed by $\omega = L$. On the other hand, Fig. A3 shows how the eigenvalue of the Laplace tidal equation, λ , and its derivative depend on the spin parameter s . We observe that λ is only a weak function of s for $s \gtrsim 10$.

We next analyse equation (93) to derive the expression of the period-spacing. We find from equation (12) that k_r can be regarded as a function of ω , λ and r . We can therefore introduce

$$K(r_b, \omega, \lambda) \equiv \int_{r_a}^{r_b} k_r(\omega, \lambda; r) dr. \quad (\text{A1})$$

If we express the angular frequency of the mode with radial order n as ω_n and the corresponding λ as λ_n , we obtain from equation (93)

$$K(r_b(\omega_{n+1}), \omega_{n+1}, \lambda_{n+1}) - K(r_b(\omega_n), \omega_n, \lambda_n) = \pi, \quad (\text{A2})$$

where we have assumed that r_a and $\hat{\alpha}$ are independent of the frequency. Under the assumption that the frequency difference, $|\omega_n - \omega_{n+1}|$, is small, equation (A2) can be approximated by

$$\frac{\partial K}{\partial r_b} \Delta r_b + \frac{\partial K}{\partial \omega} \Delta \omega + \frac{\partial K}{\partial \lambda} \Delta \lambda = \pi, \quad (\text{A3})$$

in which we have defined

$$\Delta r_b = r_b(\omega_{n+1}) - r_b(\omega_n), \quad (\text{A4})$$

$$\Delta \omega = \omega_{n+1} - \omega_n \quad (\text{A5})$$

and

$$\Delta \lambda = \lambda_{n+1} - \lambda_n. \quad (\text{A6})$$

Note that all of the partial derivatives in equation (A3) should be evaluated for

$$r_b = [r_b(\omega_n) + r_b(\omega_{n+1})]/2, \quad (\text{A7})$$

$$\omega = (\omega_n + \omega_{n+1})/2 \quad (\text{A8})$$

and

$$\lambda = (\lambda_n + \lambda_{n+1})/2. \quad (\text{A9})$$

Using the two relations,

$$\frac{\partial K}{\partial r_b} = k_r(\omega, \lambda; r_b) = 0, \quad (\text{A10})$$

which comes from the definition of r_b , and

$$\Delta \lambda = \frac{d\lambda}{ds} \Delta s = -s \frac{d\lambda}{ds} \frac{\Delta \omega}{\omega}, \quad (\text{A11})$$

where $\Delta s = s(\omega_{n+1}) - s(\omega_n)$, we obtain from equation (A3)

$$\Delta P = \frac{2\pi^2}{\omega} \left[\int_{r_a}^{r_b} \left(s \frac{d\lambda}{ds} \frac{\partial k_r}{\partial \lambda} - \omega \frac{\partial k_r}{\partial \omega} \right) dr \right]^{-1}, \quad (\text{A12})$$

where $\Delta P \equiv 2\pi/\omega_{n+1} - 2\pi/\omega_n$. Assuming $\omega \ll N$, which is valid in the propagative region of the high-order gravito-inertial modes (except very close to the turning points), we may approximate k_r given by equation (12) as

$$k_r \approx \frac{\sqrt{\lambda} N}{r\omega} \sqrt{1 - \frac{r^2 \omega^2}{\lambda c_s^2}}. \quad (\text{A13})$$

Substituting equation (A13) into equation (A12), we obtain

$$\Delta P \approx 2\pi^2 \left[\sqrt{\lambda} \left(1 + \frac{s}{2\lambda} \frac{d\lambda}{ds} \right) \int_{r_a}^{r_b} \frac{N}{r} \left(1 - \frac{r^2 \omega^2}{\lambda c_s^2} \right)^{-\frac{1}{2}} dr \right]^{-1}. \quad (\text{A14})$$

Although this expression is quite accurate for a wide range of the frequency (cf. Fig. A2), the frequency dependence is not separated from the integral of structure variables. We may then assume $r^2 \omega^2 / \lambda c_s^2 \ll 1$ to obtain

$$\Delta P \approx 2\pi^2 \left(\int_{r_a}^{r_b} N \frac{dr}{r} \right)^{-1} \left[\sqrt{\lambda} \left(1 + \frac{s}{2\lambda} \frac{d\lambda}{ds} \right) \left(1 + \frac{\omega^2 \delta}{2\lambda} \right) \right]^{-1}, \quad (\text{A15})$$

where δ is defined by

$$\delta \equiv \left(\int_{r_a}^{r_b} \frac{rN}{c_s^2} dr \right) \left(\int_{r_a}^{r_b} N \frac{dr}{r} \right)^{-1}. \quad (\text{A16})$$

If we set $\delta = 0$ in equation (A15), we obtain

$$\Delta P \approx 2\pi^2 \left(\int_{r_a}^{r_b} N \frac{dr}{r} \right)^{-1} \left[\sqrt{\lambda} \left(1 + \frac{s}{2\lambda} \frac{d\lambda}{ds} \right) \right]^{-1}, \quad (\text{A17})$$

which is the same expression as equation (10) of Ballot et al. (2012). Considering the approximated expression of $\lambda \approx m^2 [1 + (2ms - 1)^{-1}]$ (Townsend 2003), we can confirm that the right-hand side of equation (A17) is nearly constant for large s (see also Fig. A2). It is therefore essential to consider δ for the frequency variation of the period-spacing.

In Fig. A2, we compare the numerical solutions of equation (93) with the expressions by equations (A14), (A15) and (A17) for Kelvin g modes with $m = 1$ of the evolutionary models constructed by Saio et al. (2021). We first observe that, at each evolutionary stage (specified by X_c), the numerical solution and all of the expressions converge on the same value in the low frequency limit. We actually obtain from equations (A14), (A15) and (A17)

$$\lim_{s \rightarrow \infty} \Delta P = \frac{2\pi^2}{m} \left(\int_{r_a}^{r_b} N \frac{dr}{r} \right)^{-1} \quad (\text{A18})$$

in which r_b essentially means the radius of the base of the near-surface convective zone. The limiting value given by equation (A18) corresponds to Π_0 introduced by equation (21). We next find that equation (A17) poorly describes the frequency dependence of ΔP because it provides almost constant values (dotted curves). On the other hand, we notice that equation (A14) reproduces the numerical solutions within 0.2 per cent in the entire frequency range (dashed curves), and also that equation (A15) with constant r_b (fixed at the base of the convective envelope) provides good approximations to the numerical solutions only in the low frequency range (dashed-dotted curves). Particularly in the frequency ranges where the dip structure is found (the shaded areas in Fig. A2), equation (A15) differs from the numerical solutions by 0.8 per cent at most. The discrepancy between the results by equations (A14) and (A15) (dashed and dashed-dotted curves, respectively, in Fig. A2) can be explained by two reasons. One is that the approximation of $r^2 \omega^2 / \lambda c_s^2 \ll 1$, which is used to derive equation (A15), becomes inaccurate as the frequency is higher. The other is that r_b , which is assumed to be constant in equation (A15), depends on frequency in the high frequency range where r_b is fixed by $\omega = L$. The lower bound of this frequency region is indicated by the vertical line in each panel of Fig. A2. This frequency dependence of r_b is the reason for the non-monotonic variations in ΔP predicted by equation (A14). We note that the first effect (the inaccuracy of $r^2 \omega^2 / (\lambda c_s^2) \ll 1$) starts to appear in the lower frequency range than the second effect (the frequency dependence of r_b) for all the values of X_c .

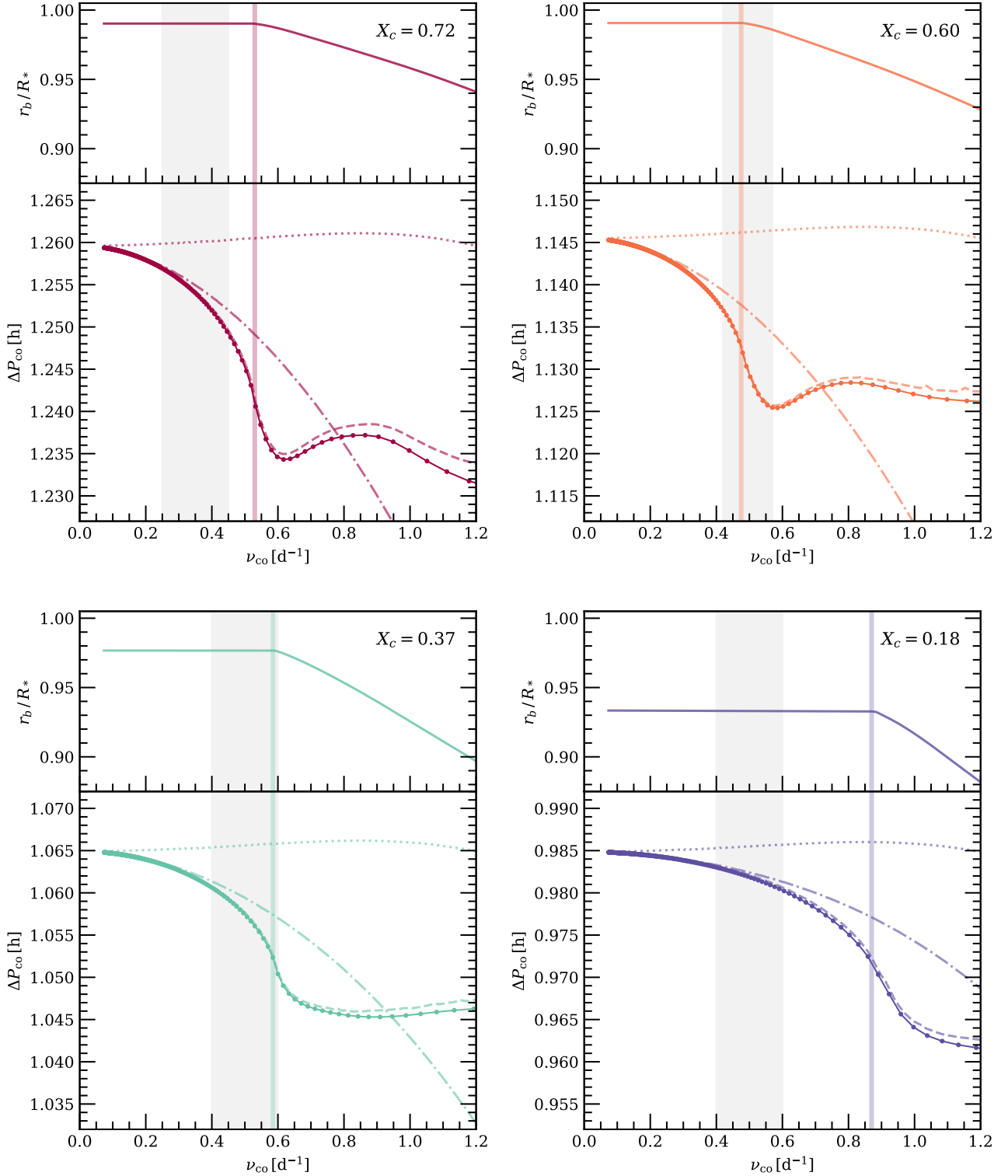


Figure A2. Frequency dependence of the period-spacing (ΔP) in the co-rotating frame and the outer boundary of the propagative cavity (r_b) of Kelvin g modes with $m = 1$ for the four evolutionary models in Fig. 4 of Saio et al. (2021) with the mass of $1.5 M_{\odot}$, the rotation period of 0.455 d and the central hydrogen mass fractions of $X_c = 0.72$ (ZAMS), 0.60, 0.37 and 0.18. (upper part of each panel) r_b in the unit of the total stellar radius R_* (solid lines) as a function of the frequency ν . The vertical line represents the boundary below and above which r_b is determined by $\omega = N$ and by $\omega = L$, respectively. (lower part of each panel) ν - ΔP diagram obtained by the numerical results based on equation (93) (the filled circles connected by solid lines). Note that ν means the reciprocal of the average period of two neighbouring solutions $[(P_{n+1} + P_n)/2]^{-1}$. The dashed, dashed-dotted and dotted curves are drawn based on equations (A14), (A15) and (A17), respectively. We fix r_b at the base of the convective envelope in equation (A15). The grey shaded zone corresponds to the area where the dip structure is located.

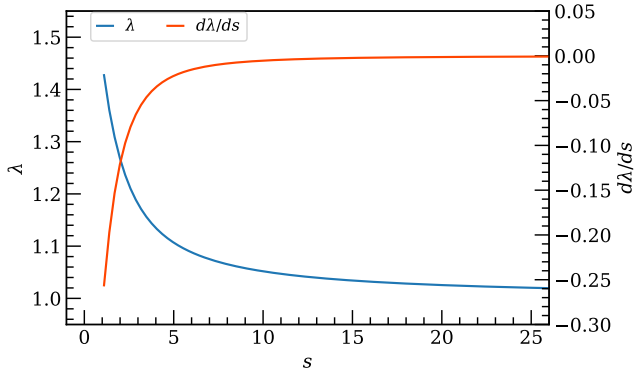


Figure A3. Eigenvalue of the Laplace tidal equation λ (blue line) and its derivative $d\lambda/ds$ (orange line) as a function of the spin parameter s in the case of Kelvin g modes with the azimuthal order of 1.

Table B1. The setting of the stellar evolution code MESA in the calculation of this paper.

Control name	Our setting
initial_mass	1.4, 1.5, 1.6 or 1.8 M_{\odot}
initial_Z	$Z = 0.02$
use_Type2_opacities	True
default_net_name	'basic.net'
atm_T_tau_relation	'Eddington'
mixing_length_alpha	$\alpha_{\text{MLT}} = 1.8$
MLT_option	'Heney'
do_element_diffusion	True
mesh_delta_coeff	0.25
max_years_for_timestep	10^6 yrs
diffusion_rtol_for_solve	10^{-5}
diffusion_atol_for_solve	10^{-6}
use_Ledoux_criterion	False or True
do_conv_premix	True

APPENDIX B: CALCULATION OF $\tilde{\epsilon}$

We construct evolutionary models of main-sequence stars with the solar composition by the MESA evolution code (r12778). Our settings of major parameters are listed in Table B1. As for the convective mixing, we try the following two cases: (1) `use_Ledoux_criterion` and `do_conv_premix` are set to false and true, respectively (cf. Paxton et al. 2019); (2) the both parameters are set to true. We refer to the first and second cases as the Schwarzschild case and the Ledoux case, respectively. Note that, in the both cases, the neutrality condition of the Schwarzschild criterion for convection is approximately satisfied in the radiative layers just outside the convective core because of the convective premixing. The other parameters are set following the test-suite 1.5M_with_diffusion, which includes element diffusion from gravitational settling and chemical diffusion.

In Fig. B1, we plot for the Schwarzschild case the profiles of (normalised) Brunt-Väisälä frequency $\sqrt{N^2 r/g}$, hydrogen mass fraction X_{H} and density ρ for different values of hydrogen mass fraction at the centre X_c . Since N^2 increases very steeply from essentially zero to a large positive value at the inner edge of the radiative envelope,

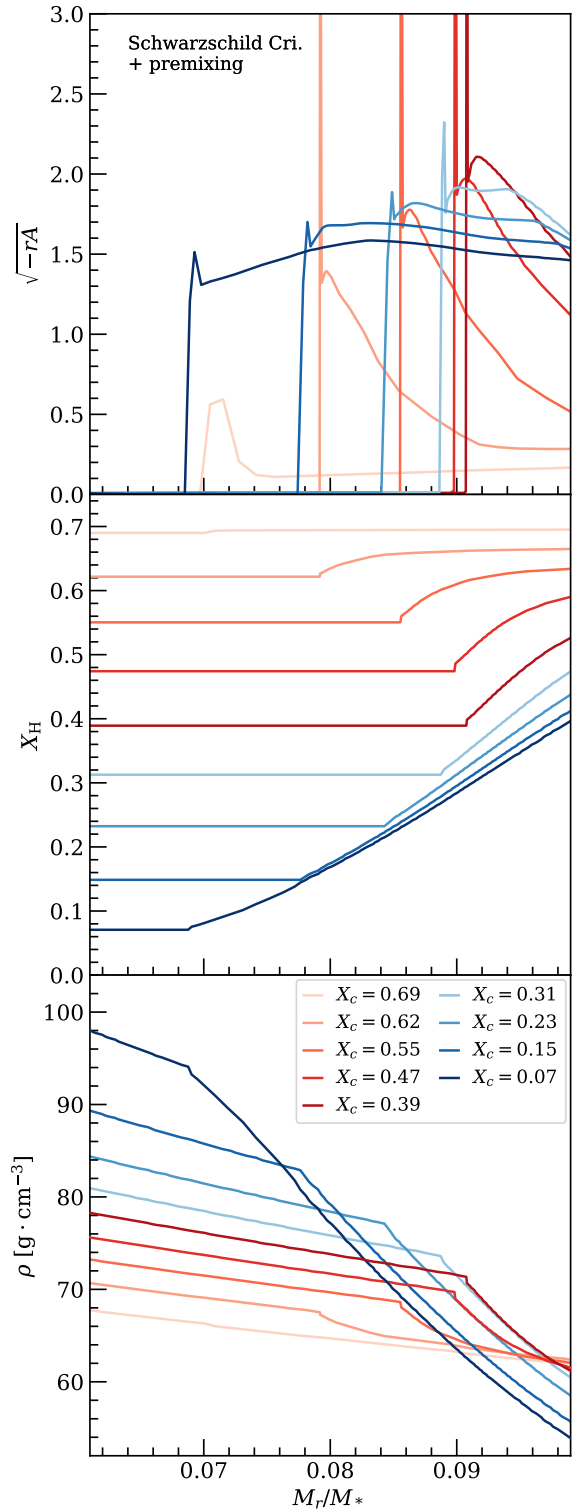


Figure B1. Profiles of the normalised Brunt-Väisälä frequency $\sqrt{-rA}$ ($\equiv \sqrt{N^2 r/g}$) (upper panel), the hydrogen mass fraction X_{H} (middle panel) and the density ρ (lower panel). These are computed by MESA with the mass of 1.5 M_{\odot} for various values of the central hydrogen mass fraction, X_c , which is equal to 0.70 at the zero-age main-sequence (ZAMS) stage. The abscissa means the concentric mass normalised by the stellar mass M_* . The lines with reddish colours (for $X_c \geq 0.40$) and bluish colours (for $X_c \leq 0.31$) correspond to the phases of core growth and shrinkage, respectively.

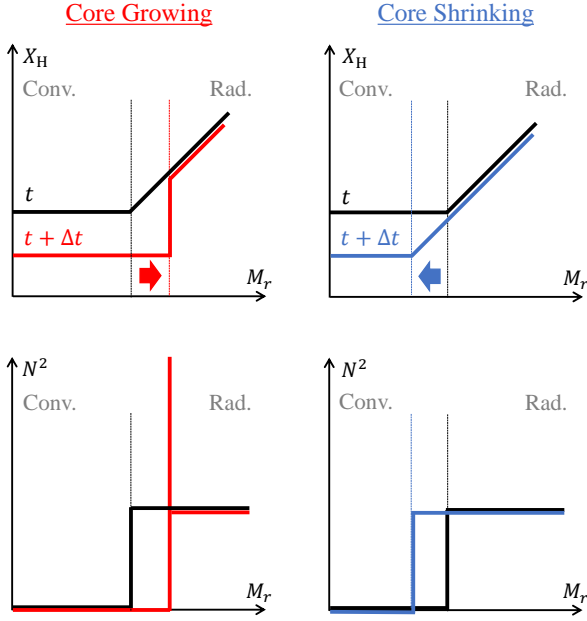


Figure B2. Schematic pictures of the evolution of X_H and N^2 profiles during the phases of core growing (left panels) and shrinking (right panels). The abscissa represents the concentric mass, while the ordinate means X_H and N^2 in the upper and lower panels, respectively. The vertical dashed lines are the boundary between the convective and radiative regions.

we can easily identify the evolutionary change in the mass of the convective core (M_{core}) from these profiles. The non-monotonic change of M_{core} for this mass range is discussed in detail in e.g. Section 3.2.3 of Aerts et al. (2010). The initial increase for $X_c \gtrsim 0.40$ is associated with the decreasing contribution of the pp chain to the core nuclear burning compared to the CNO cycle. On the other hand, the decrease of M_{core} in the later phase (for $X_c \lesssim 0.40$) is due to the gradual depletion of hydrogen, which brings about the opacity decrease, in the convective core.

Fig. B1 shows that X_H and ρ are essentially discontinuous at the boundary between the convective core and the radiative envelope when the core grows, while they are continuous when the core shrinks. This difference can be understood schematically in Fig. B2. As shown in the top left panel, X_H decreases in the core because of the nuclear burning near the centre and is homogenised to the average value due to the convective mixing. Because X_H hardly changes outside the core, it becomes discontinuous at the core boundary. When the core shrinks as in the top right panel, X_H at the outer edge of the convective core at one time becomes that at the inner edge of the radiative envelope at the next time step. Thus, X_H near the inner edge of the radiative envelope essentially records the core values in the past. It is therefore continuous. The corresponding profiles of N^2 are shown in the bottom panels. The most conspicuous difference between the two panels is that a sharp spike appears at the boundary only when the core grows (bottom left panel) because N^2 depends on the spacial derivative of X_H in the radial direction.

In any case, the scale height of the structure at the boundary is found to be so short compared to the wavelength of oscillations in the radiative side of the boundary that the derivative of ρ can be regarded as discontinuous at the boundary (cf. Appendix C). We therefore apply the results of the discontinuous case in Section 3.5 to compute $\bar{\epsilon}$, which is defined by equation (85).

APPENDIX C: DEPENDENCE ON MESH NUMBERS

C1 Comparison between the wavelength and the scale height

In Section 3, we developed two different types of analysis, that for continuous density profiles and that for discontinuous ones. In order to find which type should be adopted, we compare the wavelength of oscillations with the scale height of the structure.

Since the Brunt–Väisälä frequency, N , is the most important for the analysis, we pay attention to N , which changes from 0 in the outermost mesh point at radius $r = r_c$ in the convective core to a large value, N_1 , in the innermost mesh point at $r = r_r$ in the radiative envelope. We may therefore estimate the scale height as

$$N_1 \times \frac{r_r - r_c}{N_1 - 0} = \Delta r, \quad (\text{C1})$$

where $\Delta r = r_r - r_c$ is the radius difference between the two mesh points. We thus adopt the mesh size Δr as the scale height of the structure in the radiative layer just outside the convective core. Fig. C1 shows the comparison between the mesh size and the wavelength for two typical models with different total mesh numbers of 869 and 3375. The model with the coarse mesh is obtained with the default settings of MESA, while the fine-mesh model is constructed with the settings described in Appendix B.

From this figure, we confirm that the wavelength is much longer in the radiative envelope by about two orders of magnitude or more irrespectively of the total mesh number. We should therefore adopt the case of discontinuous profiles at the core boundary. In addition, we find that the gravito-inertial waves are well resolved in the radiative envelope even in the coarse-mesh model.

C2 Right-hand side limit of the Brunt–Väisälä frequency

In order to calculate $\bar{\epsilon}$ from equation (85), we need to calculate N_0 , which is the right-hand limit of Brunt–Väisälä frequency at the convective-core boundary (see equation 78). For simplicity, when a sharp spike appears at the boundary in the N profile (cf. the bottom left panel of Fig. B2), we choose the value at the next mesh point on the right-hand side of the spike as the right-hand limit. We identify the spike if N^2 has a local maximum that is twice or more larger than the values at the next mesh points on both sides. On the other hand, when no spike is located (cf. the bottom right panel of Fig. B2), we adopt the local maximum of N around the boundary as the right-hand side limit.

Note that the intermediate convection zones sometimes arise in the layers of chemical composition gradients when the core grows in the MESA calculation particularly if the Schwarzschild criterion for convection is adopted. In that case, we regard the outer boundary of the outermost intermediate convection zone as the core boundary in the above method.

Fig. C2 shows the profiles of normalised Brunt–Väisälä frequency ($\sqrt{r/g}N$) for two different spatial mesh numbers with the estimated right-hand side limits at the core boundary. We regard that the model with the mesh number of 3388 has a spike, while that with 878 does not. The reason for no spike in the latter model is that the spatial resolution is too low to resolve the rapid change in the gradient of chemical compositions around the core boundary. In spite of this difference, there is little influence on the estimate of N_0 in these particular examples.

On the other hand, Fig. C3 shows the evolution of $\bar{\epsilon}$ and M_{core} for two different settings about the mesh numbers. The blue lines are obtained from the coarse-mesh models with the default settings of

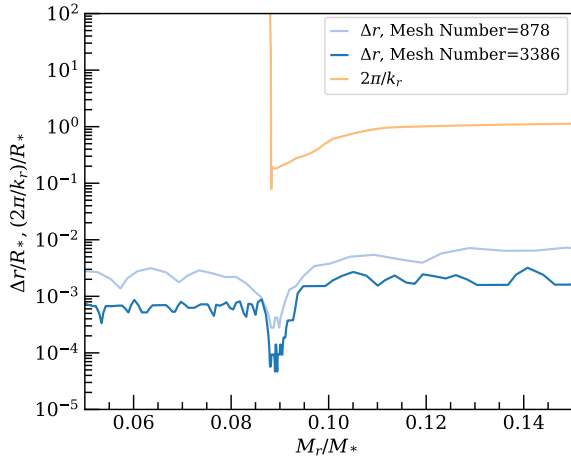


Figure C1. Comparison between the mesh size Δr (blue lines) and the wavelength $2\pi/k_r$ (orange line) computed by MESA with the mass of $1.5 M_\odot$ as functions of the fractional mass (M_r/M_*). The vertical axis is normalised by the stellar radius. The mesh size is plotted for the two models with different total mesh numbers of 869 (deep blue line) and 3375 (light blue line). Both models have $X_c = 0.51$, which corresponds to the age of 0.80 Gyr. The wavelength is computed for the finer-mesh model with the spin parameter of $s = 10$ and the rotation period of 0.455 d.

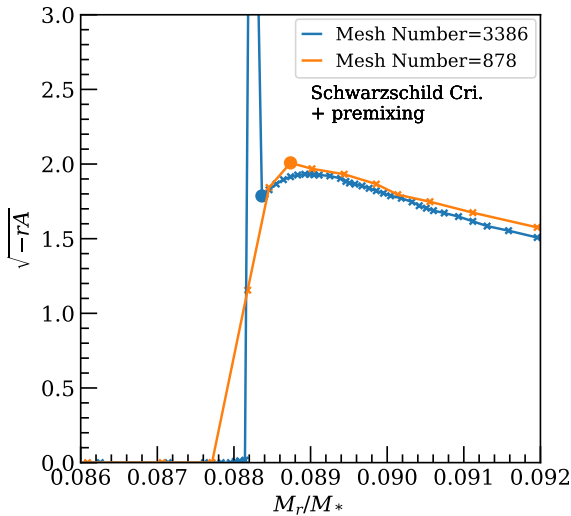


Figure C2. Profiles of the normalised Brunt-Väisälä frequency $\sqrt{-rA} = \sqrt{r/gN}$ as functions of the fractional mass (M_r/M_*) computed by MESA with the mass of $1.5 M_\odot$ and $X_c = 0.51$ (which corresponds to the age of 0.80 Gyr). The blue and orange lines correspond to the cases of the total mesh number of 3388 and 878, respectively. The small crosses represent the positions of mesh points, while the large filled circles indicate the mesh points at which the right-hand limits of N at the core boundary are estimated.

MESA, whereas the orange lines correspond to the fine-mesh models constructed with the settings described in Appendix B. There is little difference in M_{core} between the two cases, whereas a distinct discrepancy in $\bar{\epsilon}$ is found for $0.58 \lesssim X_c \lesssim 0.68$. The discrepancy is also because of the too poor spatial resolution of the coarse-mesh models to resolve the variation in chemical compositions. These examples demonstrate the importance of having sufficient mesh points in models to compute $\bar{\epsilon}$ precisely.

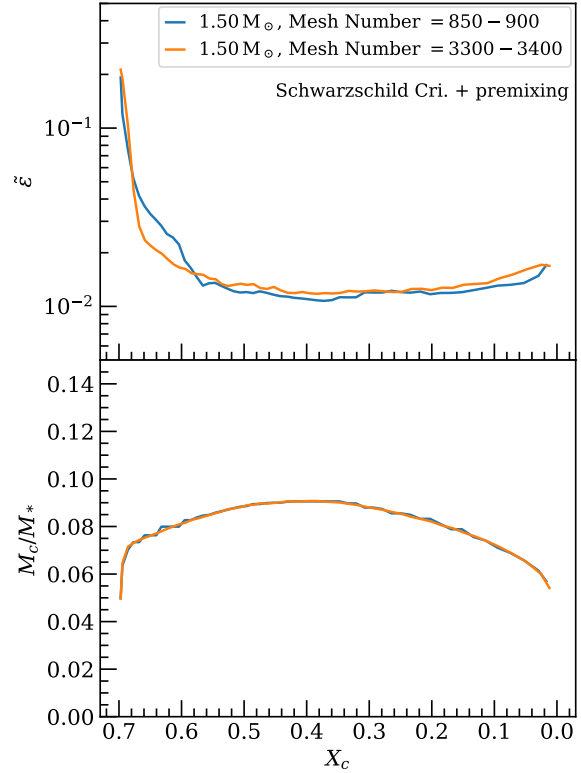


Figure C3. Evolution of $\bar{\epsilon}$ and M_{core} as function of the central hydrogen mass fraction X_c for the models with $1.5 M_\odot$. We set the rotation period to 0.455 d. The ordinates represent $\bar{\epsilon}$ (upper panels) and M_{core} normalised by the total stellar mass M_* (lower panels). The blue and orange lines correspond to the models with coarse and fine mesh points, respectively (refer to the main text for the details). In the both cases, the Schwarzschild criterion for convection is adopted, and the convective premixing is taken into account. Note that X_c is equal to 0.70 at the zero-age main-sequence stage and decreases during the evolution afterwards.

This paper has been typeset from a $\text{\TeX}/\text{\LaTeX}$ file prepared by the author.